Tabulated chemistry approach for diluted combustion regimes with internal recirculation and heat losses

Jean Lamouroux [a], Matthias Ihme [b], Benoit Fiorina [a,*], Olivier Gicquel [a]

[a] EM2C – CNRS, Ecole Centrale Paris, Châtenay Malabry, France
[b] Department of Mechanical Engineering, Stanford University, Stanford, CA 94305, USA

ABSTRACT

An efficient solution to reducing NO_x formation is to maintain a relatively low flame temperature. This can be achieved by mixing reactants, prior to combustion, with chemically inert diluents such as cooled combustion products. In such diluted combustion systems, the flame temperature decreases because of thermal ballast, limiting NO_x production. This work focuses on modeling the specifics of this combustion regime in confined combustors. To characterize the dilution of reactants by burnt gases, the importance of complex chemistry effects is emphasized and taken into account using a detailed chemistry tabulation approach. This approach extends the flamelet/progress variable formulation by including information about the intensity of internal dilution rates and heat losses. A turbulent combustion model is then developed in a large eddy simulation (LES) framework. The combustion model is validated by considering two combustor configurations, namely an adiabatic burner and a combustor having isothermal walls – both operating under highly diluted combustion conditions. Simulation results are in good agreement with experimental data, confirming the importance of detailed chemistry information and the validity of the tabulation approach to LES application to diluted combustion.

© 2014 The Combustion Institute. Published by Elsevier Inc. All rights reserved.

1. Introduction

The energetic efficiency of combustion systems can be enhanced by transferring heat from exhaust products to the fresh gases by means of regenerative heating. Unfortunately, the resulting increase in the reactant temperature has an adverse effect on the formation of nitrogen oxides (NO_x). An efficient solution to reducing NO_x formation is to maintain a relatively low flame temperature. This can be achieved by mixing reactants with chemically inert diluents such as combustion products. In "diluted combustion" systems, the flame temperature decreases because of thermal ballast, limiting NO_x production. These systems promote different combustion regimes such as MILD (moderate or intense low-oxygen dilution) combustion [1,2], flameless oxidation [3] and high-temperature air combustion (HiTAC) [4,5].

In diluted combustion technologies, reactants are diluted with large amounts of burnt reaction products prior to combustion, which enables flame stabilization under lean conditions, thereby avoiding high-temperature regions that promote enhanced

thermal NO_x formation. Experimental and numerical studies have been conducted in confined systems such as HiTAC combustion chambers [6,7], the IFRF (International Flame Research Foundation) semi-industrial-scale configurations [8–10], and reverse flow configurations [11,12]. These diluted combustion technologies exhibits strong recirculation zones that enhance the mixing between fresh and burnt streams. Local stoichiometric conditions are avoided, so that NO_x production is dramatically decreased. It is noteworthy that diluted combustion can be achieved without internal recirculation of burnt gases: for example, Dally et al. [13] reproduced oxygen-diluted and MILD combustion regimes in a Jet in Hot Coflow (JHC) experiment.

A schematic of the model problem of diluted combustion with internal product gas recirculation in a confined burner geometry is shown in Fig. 1. The schematic illustrates the modification in the composition of reactants, which strongly varies with recirculation and dilution by burnt gases.

A major issue in the modeling of diluted combustion is the pronounced sensitivity of the flame structure to the reaction chemistry [14,15]. To illustrate the importance of the detailed chemistry when a gas mixture is subjected to dilution by hot reaction products, a series of adiabatic laminar flames are computed. These simulations consider chemical representations of increasing

---

* Corresponding author. Fax: +33 (1)47028035.
E-mail address: benoit.fiorina@ecp.fr (B. Fiorina).

Nomenclature

Latin
C	normalized progress variable
D	molecular diffusivity
H	specific mixture enthalpy
S_Z	mixture fraction unmixedness factor
T	temperature
Y_c	progress variable
Y_D	dilution variable
Y_e	elemental mass fraction
Y_k	species mass fraction of species k
Z	mixture fraction
$\mathcal{Z}$	mixture fraction normalized with respect to undiluted compositions

Greek
α	dilution parameter
β	heat loss parameter
Λ	progress parameter
ρ	density

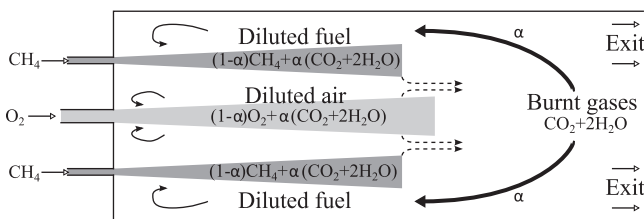|	
ϕ	equivalence ratio
ϕ_G	global equivalence ratio
χ	scalar dissipation
$\boldsymbol{\psi}$	vector of chemical quantities
$\dot{\boldsymbol{\omega}}$	vector of chemical reaction rates, expressed in s^{-1}
$\dot{\omega}_k$	chemical reaction rate of species k, expressed in s^{-1}

Superscripts
Dil	diluent stream
F	fuel stream
Ox	oxidizer stream
0	undiluted conditions

Subscripts
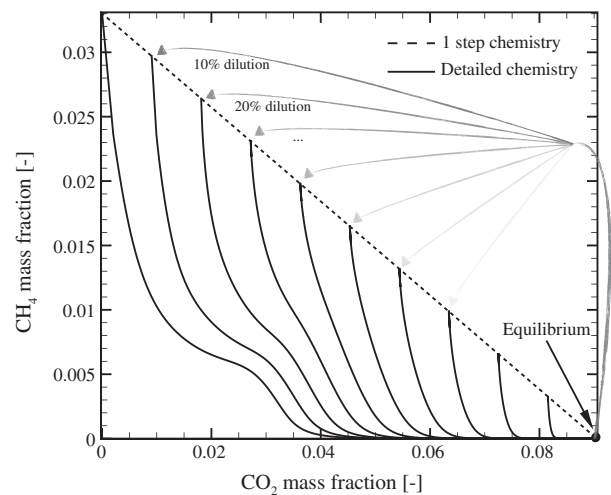|	
G	global equivalence ratio conditioning
$\vert_{\alpha=0}$	undiluted-conditioned quantity
$\vert_{\beta=0}$	quantity evaluated without heat losses ($\beta = 0$)
$\vert_{\beta=1}$	quantity evaluated for maximal heat losses ($\beta = 1$)

complexity, namely the infinitely fast chemistry approximation, a one-step irreversible chemistry, and a detailed reaction sequence. The problem configuration consists of a steady-state counterflow methane/air diffusion flame, and different values of strain rates (including the stable and the unstable branch) are considered. Both reactant streams are diluted with burnt products, having a composition that is identical to that of the MILD combustor configuration studied by Verissimo et al. [16] (see Section 5.1). Chemical trajectories in CO_2-CH_4 composition space are presented in Fig. 2 for different dilution levels. Results obtained with the detailed GRI 3.0 mechanism [17] are shown by solid lines, the dashed line corresponds to the one-step irreversible chemistry, and the limiting case of infinitely fast chemistry is shown by the symbol. From this figure it can be seen that the detailed chemistry solution exhibits several possible trajectories, which depend on the level of dilution. In contrast, the single-step chemistry trajectory is not sensitive to the dilution level, so the CH_4 mass fraction exhibits a linear dependence on Y_{CO_2}. Since the infinitely fast chemistry model assumes that the mixture is always at equilibrium state, the chemical trajectory reduces to a single point for a given value of equivalence ratio. Results from the detailed chemistry solution show that the chemistry is affected by dilution, impacting fundamental flame properties, including flame structure, species composition, and pollutant emission.

An attractive strategy for including detailed chemistry effects using moderate CPU resources are tabulated chemistry techniques

[18–22]. Among these, the flamelet model for nonpremixed combustion assumes that a turbulent flame can be decomposed into a collection of one-dimensional flame elements [18]. Each flamelet is then represented by a reaction–diffusion element that is constructed between oxidizer and fuel streams. In the original formulation, proposed by Peters [18], the fuel and oxidizer composition are assumed to be constant for each flame element. By construction, this two-stream formulation is not able to account for effects of reactant dilution by burnt gases on the chemical flame structure. To overcome this issue, a three-stream flamelet-progress variable (FPV) approach has recently been developed [23]. This model was applied to large eddy simulations of a Jet-in-Hot-Coflow (JHC) burner [23,24], in which the burner was operated in the recirculation-free adiabatic MILD operating regime. The dilution

Fig. 1. Model problem of a diluted combustion configuration with internal recirculation of burnt gases. Considering the idealized problem of methane/oxygen combustion, the initially separated reactants mix and react to produce CO_2 and H_2O. Reaction products are then recirculated where they modify the composition in the oxidizer and fuel streams. The product gas dilution level is denoted by α.

Fig. 2. Chemical trajectories in CO_2–CH_4 state space for different dilution levels, illustrating the sensitivity of the fuel conversion to the reaction chemistry and the dilution. Here, the diluent is composed of the equilibrium product-gas composition for an equivalence ratio of $\phi = 0.58$. Trajectories are extracted from steady laminar counterflow diffusion flame computations, from the pure mixing line to the fully burnt states.

is provided by a hot coflow stream, so the diluted reactant composition does not vary in the combustion chamber. A model that uses two independent mixture fractions is therefore sufficient to capture the flame properties [23]. Nonetheless, when the dilution process is induced by strong internal recirculation, the local composition of the diluted fuel or oxidizer stream changes in time and space, and the use of passive scalars to describe the mixture variations is not adequate any more.

The present work presents a modeling route to account for the effect of fresh-gas dilution by burnt products on the dynamics and structure of turbulent flames. This approach is applied to the prediction of "diluted combustion" systems, including for instance MILD (moderate or intense low-oxygen dilution) combustion [1,2] or flameless oxidation [3] regimes. To this end, a tabulation methodology based on the FPV method, which accounts for effects of internal dilution on the chemical flame structure, is first introduced. Since heat losses are important in most practical combustors, the impact of these effects on the chemistry will also be considered. Two tabulation strategies that differ in the representation of heat transfer and dilution are considered. A sub-grid-scale model for the turbulence/flame interaction is proposed, and a semiempirical model is developed to represent the production and internal recirculation of diluents. The capability of this LES combustion model is demonstrated in two combustor configurations, namely an adiabatic burner and a combustor that utilized isothermal wall treatment. These configurations were experimentally investigated at the Instituto Superior Técnico of Lisbon [25,16]. Both burners feature severe internal recirculation, very low pollutant emissions, and high combustion efficiency. Comparisons with experimental data are then carried out, and the validity of the proposed model is discussed.

2. Modeling of diluted combustion

2.1. Influence of fresh gas dilution on the chemical trajectories

The equilibrium thermochemical state is identified from the element composition and the enthalpy h. Under unity Lewis number assumption, the pair (Z, H), where Z is the mixture fraction and H the mixture enthalpy, is then sufficient to capture the equilibrium state of the mixture, whether or not fresh gases have been diluted by burnt gases. This is, however, not the case for reaction processes that are strongly affected by the rate of fresh gas dilution. To illustrate this, we consider a 0-D constant-pressure perfectively stirred reactor (PSR), which is described by the following set of governing equations:

$$\rho \frac{\partial Y_k}{\partial t} = \frac{\rho}{\tau}\left(Y_k^b - Y_k\right) + \rho \dot{\omega}_k$$
$$\rho C_p \frac{\partial T}{\partial t} = \frac{\rho}{\tau}\left(\sum_{k=1}^K Y_k^b H_k^b - \sum_{k=1}^K Y_k^b H_k\right) - \sum_{k=1}^K \rho \dot{\omega}_k H_k \tag{1}$$

The inlet mass flow rate $\dot{m}$ and the residence time τ are related to the volume V of the reactor through the relation $\dot{m} = \rho V/\tau$. The reactor is initially fed with a mixture of fresh gases at temperature $T(t=0)$ and composition $Y_k(t=0)$. Under constant-pressure conditions, this mixture reaches the equilibrium state, denoted by superscript b. At $t=0$, gases of temperature T^b and composition Y_k^b are injected into the reactor and dilute the fresh gas mixture. As the elemental composition of the mixture is kept constant during the dilution process, the thermochemical equilibrium state is not affected. A series of PSR simulations are performed with the following initial gas composition and temperature: $Y_{O_2} = 0.14253$, $Y_{CH_4} = 0.00214$, $Y_{N_2} = 0.75633$, $Y_{H_2O} = 0.099$, and $T = 1330$ K, and using the GRI 3.0 mechanism [17]. Figure 3 shows the solutions of Eq. (1) projected in the (Y_{CO}, Y_{CO_2}) chemical subspace. Each curve
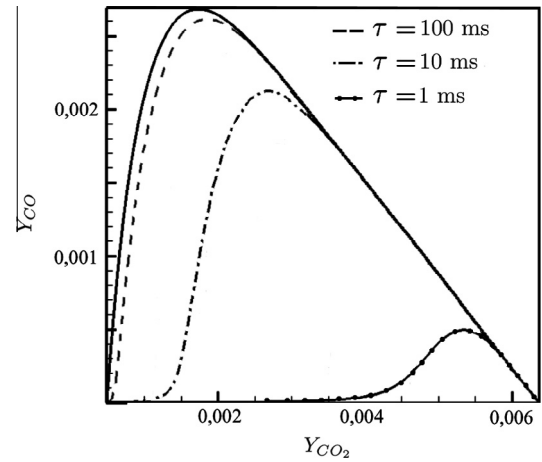

Fig. 3. Y_{CO} evolution as a function of Y_{CO_2} during autoignition of a PSR for several residence times τ. The solid trajectory corresponds to the 0-D reactor computation (with $\tau \to \infty$ in Eq. (1)).

corresponds to a given residence time τ of the gases inside the reactor. The solid line represents the chemical trajectory of a homogeneous reactor (solution of Eq. (1) with $\tau \to \infty$). For a long residence time ($\tau = 100$ ms), the chemical trajectory rapidly converges toward the closed reactor solution, and the fresh gases dilution by burnt gases does not significantly affect the CO production. However, for shorter residence times ($\tau = 10$ ms and $\tau = 1$ ms), trajectories differs. The dimension of the attractive manifold increases and a chemistry tabulation function limited to a single progress variable (here CO_2) is not sufficient to capture the chemical processes. A solution to include dilution effects in the FPV model is presented in the following section.

2.2. Chemistry tabulation

2.2.1. Flamelet/progress variable approach

In the FPV approach, the turbulent flame is locally seen as a collection of one-dimensional laminar counterflow diffusion flames. Assuming steady combustion and neglecting preferential diffusion effects, the structure of these flame elements is then described by the solution of the flamelet equations, which are here written as

$$-\frac{\chi_Z}{2}\frac{\partial^2 \psi}{\partial Z^2} = \dot{\omega}, \tag{2}$$

where Z is the mixture fraction, ψ is a vector composed of all species mass fractions $\mathbf{Y}$ and temperatures T, and the vector $\dot{\omega}$ denotes their respective source terms. $\chi_Z = 2D \mid \nabla Z \mid^2$ is the scalar dissipation rate of the mixture fraction, which introduces the molecular diffusivity D of the mixture. Since the focus of this investigation is the diluted combustion of a methane/air mixtures, we assume equal diffusivities for all species.

To accommodate variations in the reactant stream compositions, Eqs. (2) are supplemented by the following boundary conditions:

$$\psi(Z = 0) = \psi^{Ox}, \tag{3}$$
$$\psi(Z = 1) = \psi^F, \tag{4}$$

where the superscripts F and Ox denote, respectively, boundary conditions in the fuel stream and in the oxidizer stream. Thermochemical quantities are then functions of the mixture fraction and the scalar dissipation rate. However, this parameterization does not ensure a unique thermochemical state space representation, since for given values of χ_Z, stable, unstable, and unburned states

may coexist. To overcome this issue, a reaction progress parameter Λ has been introduced [22,26], which provides a unique representation of the entire thermochemical state space. The progress parameter is defined through a progress variable Y_c, which can be evaluated as the solution of a minimization problem [27]. A definition for Y_c in the context of methane/air combustion is

$$Y_c = Y_{CO_2} + Y_{CO} + Y_{H_2} + Y_{H_2O}. \tag{5}$$

Y_c and Z are by definition statistically dependent. To facilitate the estimation of the joint presumed probability density function (PDF) for the turbulent closure, the variable Λ is introduced. Λ is evaluated by conditioning Y_c at a given value of the mixture fraction Z^*,

$$\Lambda = Y_c|_{Z^*}, \tag{6}$$

and the thermochemical vector ψ is a function of mixture fraction and progress parameter:

$$\psi = \mathcal{F}_\psi(Z, \Lambda). \tag{7}$$

Since the balance equation for Λ is difficult to close for turbulent flows, it is preferable to solve a transport equation for the progress variable Y_c. The function $\mathcal{F}_{Y_c}$, which relates Y_c to Z and Λ, is identified by using Eqs. (5) and (7):

$$Y_c = \mathcal{F}_{\mathcal{Y}_c}(Z, \Lambda). \tag{8}$$

Every thermochemical quantity contained in ψ evaluated in the steady flamelet equations is therefore expressed as

$$\psi = \mathcal{F}_\psi(Z, \mathcal{F}_{Y_c}^{-1}(Z, Y_c)) = \mathcal{G}_\psi(Z, Y_c). \tag{9}$$

2.2.2. Diluted flamelet/progress variable approach

Capturing dilution effects in a flamelet-based tabulated chemistry framework implies first modeling the mixing of the fresh reactants with the burnt product gases. As mentioned previously, assuming equilibrium state, the burnt gas composition and temperature depend only on the mixture fraction and enthalpy under a unity Lewis number assumption. These reaction products may mix at different rates with the fresh oxidizer and/or the fuel streams, multiplying the number of possible configurations. The degrees of freedom underlying these processes are so numerous that a direct tabulation of flamelets for all dilution configurations is in practice not feasible. However, reasonable simplifications can be made as in confined burners, the dilution is accomplished by large-scale recirculation of burnt gases. Therefore, diluted combustion can be represented as a three-stream problem, consisting of a fuel stream, an oxidizer stream, and an internal reaction product gas stream. Because of large residence time in the recirculation zones, the burnt gas composition corresponds to the chemical equilibrium of a fuel/oxidizer mixture that is characterized by the global equivalence ratio ϕ_G. These large time scales also favor heat exchanges between recirculating burnt gases and burner side-walls. Therefore, the diluent composition is in practice mainly a function of the global equivalence ratio and the level of wall heat transfer.

The study by Abtahizadeh et al. [28] showed that the dilution process has a direct effect on the flame structure. In terms of chemistry tabulation, accounting for the influence of diluent gradients considerably increases the dimensionality of the tabulated manifold. In the approach developed here, we will neglect the influence of these gradients on the flame structure.

By these assumptions, boundary conditions of the system of Eq. (2) are reformulated to account for the effect of dilution on the flamelet archetype that is used for the chemistry tabulation. The counterflow flamelet boundary conditions now read

$$\psi(Z = 0) = \psi^{Ox}(\alpha, \beta), \tag{10}$$

$$\psi(Z = 1) = \psi^{F}(\alpha, \beta), \tag{11}$$

where α is the dilution parameter and β is the heat loss parameter.

A schematic of representative flame-configurations and definitions of the dilution and heat-loss parameters is shown in Fig. 4.

The dilution parameter α is defined as the mass ratio between fresh reactants and diluents: $\alpha = 0$ in the absence of diluents and $\alpha = 1$ when the mixture is saturated with diluents.[1] To identify the composition of the diluent stream, we introduce Y_k^{Dil}, denoting the mass fraction of species k in the diluent stream. In practice, the diluent mixture composition Y_k^{Dil} is evaluated from the thermochemical equilibrium state of the mixture under global equivalence ratio conditions. Denoting by Y_k^{F} and Y_k^{Ox} the mass fractions of species k in the fuel and oxidizer streams, the definition of α reads

$$\alpha = \frac{Y_k^{F} - Y_k^{F,0}}{Y_k^{Dil}(\beta) - Y_k^{F,0}} = \frac{Y_k^{Ox} - Y_k^{Ox,0}}{Y_k^{Dil}(\beta) - Y_k^{Ox,0}}, \tag{12}$$

and the superscript ",0" denotes the undiluted mixture.

The heat loss parameter β is introduced to consider nonadiabatic effects. This parameter is equal to zero under adiabatic conditions and $\beta = 1$ when heat losses are maximum. By denoting as H^{Dil} the enthalpy (sum of chemical and sensible enthalpies) of the diluent, the definition of β is written as

$$\beta = \frac{H^{Dil} - H^{Dil}|_{\beta=0}}{H^{Dil}|_{\beta=1} - H^{Dil}|_{\beta=0}}. \tag{13}$$

From this definition, the composition and enthalpy of the diluted reactant streams (fuel and oxidizer) can be deduced:

$$Y_k^{F}(\alpha, \beta) = \alpha\left(Y_k^{Dil}(\beta) - Y_k^{F,0}\right) + Y_k^{F,0}, \tag{14}$$

$$H^{F}(\alpha, \beta) = \alpha\left(H^{Dil}(\beta) - H^{F,0}\right) + H^{F,0}, \tag{15}$$

$$Y_k^{Ox}(\alpha, \beta) = \alpha\left(Y_k^{Dil}(\beta) - Y_k^{Ox,0}\right) + Y_k^{Ox,0}, \tag{16}$$

$$H^{Ox}(\alpha, \beta) = \alpha\left(H^{Dil}(\beta) - H^{Ox,0}\right) + H^{Ox,0}, \tag{17}$$

and H^{Dil} is written as

$$H^{Dil}(\beta) = \beta\left(H^{Dil}|_{\beta=1} - H^{Dil}|_{\beta=0}\right) + H^{Dil}|_{\beta=0}. \tag{18}$$

The minimal enthalpy of the diluent enthalpy $H^{Dil}|_{\beta=1}$ corresponds to the enthalpy of the diluent mixture that is cooled to a specified minimum temperature T_{min}^{Dil}. In the following this temperature is associated with the burner wall temperature.

When all thermochemical quantities are parameterized in terms of mixture fraction, progress variable, dilution parameter, and heat-loss parameter, ψ evolves in a four-dimensional subspace. In analogy to Eq. (9), this is written as

$$\psi = \mathcal{G}_\psi(Z, Y_c, \alpha, \beta), \tag{19}$$

and this formulation is referred to as diluted flamelet/progress variable (DFPV) approach.

---

[1] Unlike [23], this dilution parameter is not a second mixture fraction. It tracks the deviations, induced by dilution, of the chemical trajectories projected in a constant Z plane.
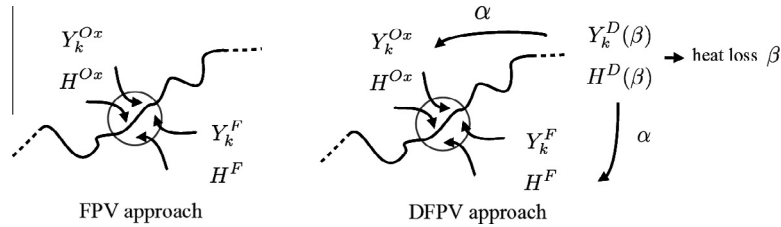
Fig. 4. Schematic representation of the different constraints imposed on temperature and species of the boundary conditions used to generate counterflow diffusion flames; left: FPV model; right: DFPV model.

2.3. Relations between controlling scalars

All control parameters that appear in Eq. (19) are evaluated from transported quantities. The mixture fraction Z is defined from a set of element mass fractions Y_e [29]:

$$Z = \frac{Y_e - Y_e^{Ox}(\alpha)}{Y_e^F(\alpha) - Y_e^{Ox}(\alpha)}. \tag{20}$$

Since the fuel and oxidizer elemental species mass fractions ($Y_e^F(\alpha)$ and $Y_e^{Ox}(\alpha)$ respectively) are functions of the dilution ratio, the balance equation for Z exhibits unclosed dependencies. To avoid the dependency on the dilution parameter, we introduce a mixture fraction formulation, which is defined with respect to the undiluted mixture composition, and therefore independent of α. This quantity is denoted by $\mathcal{Z}$ and has the following definition:

$$\mathcal{Z} = \frac{Y_e - Y_e^{Ox}|_{\alpha=0}}{Y_e^F|_{\alpha=0} - Y_e^{Ox}|_{\alpha=0}}. \tag{21}$$

As such, $\mathcal{Z}$ can be directly evaluated by solving a conserved scalar transport equation. Furthermore, by introducing the mixture fraction $\mathcal{Z}_G$, which is evaluated under global equivalence ratio conditions (20) and (21) are related as

$$Z = \frac{\mathcal{Z} - \alpha \mathcal{Z}_G}{1 - \alpha}. \tag{22}$$

Figure 5 illustrates temperature profiles as a function of mixture fraction $\mathcal{Z}$ and different values of reaction progress Y_c and dilution levels. In this configuration, the oxidizer consists of preheated air at 600 K and the fuel stream consists of methane at ambient temperature. The diluent is composed of burnt reaction products at an equivalence ratio of $\phi = 0.77$ without any heat losses ($\beta = 0$). The chemistry is described by the GRI 3.0 mechanism [17]. The flame structure is obtained from steady laminar flamelet computations using the FLAMEMASTER code [30]. This figure shows that the range

in mixture-fraction space decreases with increasing dilution, until it reaches a singular point that is defined by the pure diluent mixture.

The heat loss parameter, β, is linked to the enthalpy, H, which is expressed in the Z-mixture fraction space as

$$H(Z, \alpha, \beta) = Z\left[H^F(\alpha, \beta) - H^{Ox}(\alpha, \beta)\right] + H^{Ox}(\alpha, \beta). \tag{23}$$

Combining Eqs. (15), (17), and (22), and using the definition of β from Eq. (18), leads to

$$\beta = \frac{H - (H_{\alpha=0}^F - H_{\alpha=0}^{Ox})(\mathcal{Z} - \alpha \mathcal{Z}_G) - (1-\alpha)H_{\alpha=0}^{Ox} - \alpha H^{Dil}|_{\beta=0}}{\alpha(H^{Dil}|_{\beta=1} - H^{Dil}|_{\beta=0})}. \tag{24}$$

Note that this expression is valid for $\alpha \neq 0$, which is consistent with the underlying assumption that heat-loss and dilution effects are coupled. Consequently, $\alpha = 0$ implies $\beta = 0$.

For this approach, the rate of dilution needs to be estimated from the evaluation of the reactant composition prior to combustion. Dilution with burnt gases as well as chemical reactions will affect the progress variable Y_c, defined from Eq. (5). To discriminate the progress of reaction from dilution effects, the normalized form of the progress variable, C, is introduced,

$$C = \frac{Y_c - Y_c^0(\mathcal{Z}, \alpha, \beta)}{Y_c^{eq}(\mathcal{Z}, \alpha, \beta) - Y_c^0(\mathcal{Z}, \alpha, \beta)}, \tag{25}$$

where Y_c^{eq} and Y_c^0 represent, respectively, the value of Y_c at equilibrium and in the unburned mixture diluted at a rate α.

The dilution variable Y_d is defined from a combination of species mass fractions, chosen such that $Y_d^{F,0} = 0$ and $Y_d^{Ox,0} = 0$. The following relation between Y_d and α is then obtained from Eq. (12):

$$\alpha = \frac{Y_d}{Y_d^{Dil}(\beta)}, \tag{26}$$

$Y_d^{Dil}(\beta)$ denotes the value taken by the dilution variable Y_d in pure diluent, i.e. at equilibrium and for global equivalence ratio mixing
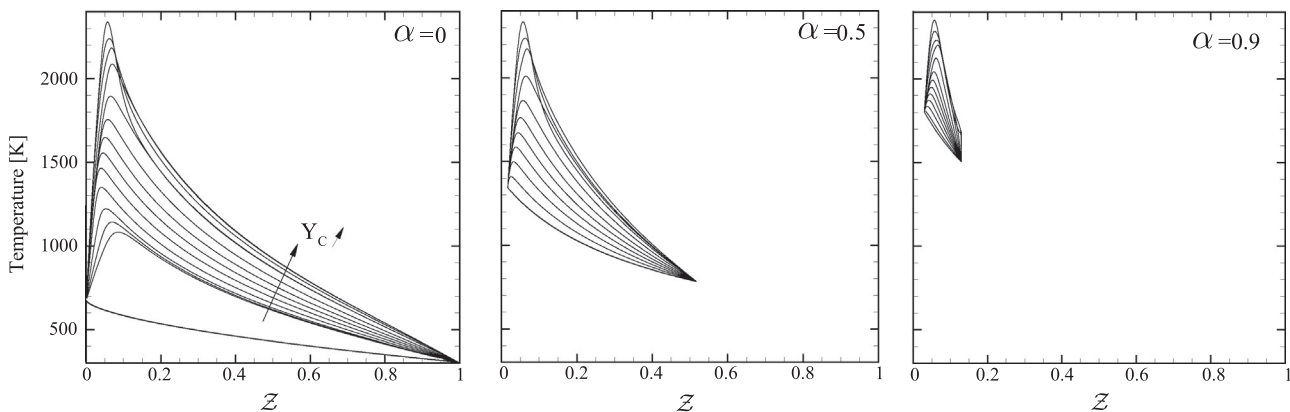
Fig. 5. Temperature profiles as function of mixture fraction $\mathcal{Z}$ for different levels of reaction progress and increasing levels of dilution levels α (from left to right).

conditions. In the following simulations the dilution variable is defined as $Y_d = Y_{CO} + Y_{CO_2}$. From gas equilibrium computations, we observed that this combination ensures a very weak dependency of Y_d^{Dil} on the heat-loss level β. The definition of α is then simplified to

$$\alpha = \frac{Y_d}{Y_d^{Dil}(\beta = 0)}. \tag{27}$$

This simplification was tested for the experimental configurations and operating conditions investigated further, and was found adequate for all mixture compositions. Yet this assumption should be investigated further for application to heavy hydrocarbon fuels, which has not been considered in this study.

2.4. Analysis of laminar flame response

In the following section, a one-dimensional analysis is presented to investigate the response of the flame structure to dilution. This analysis provides a fundamental understanding about the importance of considering dilution effects on the combustion process.

2.4.1. Dilution without heat-loss effects

Figure 6 shows simulation results for the S-shaped curve without consideration of heat losses. As expected, dilution increases the temperature of the unburned branch and the temperature of the burnt mixture converges to a unique equilibrium point. The critical conditions for the quenching and ignition scalar dissipation rates are also affected by dilution. With increasing dilution ratios, the extinction limit increases and eventually merges with the ignition point. The transition between unburned and burnt conditions is then smooth and monotonic, which is in accordance with the MILD combustion regime characterization of Oberlack & Peters [2]. Last, combustion is sustained for high scalar dissipation rates if dilution is sufficient: this explains why in most diluted combustion configurations, combustion is stabilized despite high air injection velocities. The influence of dilution on combustion is also highlighted by the species trajectories in compositional space. Figure 7 shows the evolution of mass fractions of carbon dioxide and carbon monoxide as functions of Y_c for different dilution rates and at a given mixture fraction.

From these results it can be seen that the chemical trajectories converge to an attractor space that is defined by the undiluted mixture trajectory. As noted previously, the equilibrium composition is identical for all cases, since the enthalpy of the mixture is not affected by dilution. However, despite the convergence to the
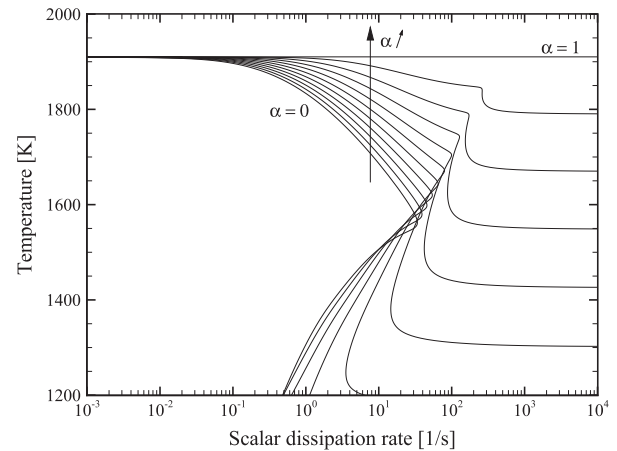
Fig. 6. Steady flamelet solution at $\mathcal{Z} = \mathcal{Z}_G$ for different dilution levels α showing temperature as function of scalar dissipation rate. The operating conditions correspond to the MILD combustion experiment of [16]. Fuel is methane at ambient temperature and air is preheated to 600 K. Global equivalence ratio is equal to $\phi_G = 0.588$ and no heat losses are considered.

same manifold, these trajectories are strongly dependent on the dilution rate. The species production rates are also strongly dependent on the dilution. This is illustrated in Fig. 8b, where the progress variable and the CO production rate are plotted as functions of Y_c.

2.4.2. Dilution with heat-loss effects

In practical burner configurations, heat losses play a crucial role in the combustion process. Figure 9 presents various sets of S-curves obtained for different values of α and diluent temperatures T^{Dil}. Independent of the level of heat losses applied to the diluent, the temperature of fresh gases increases with dilution. The equilibrium temperature, obtained for low scalar dissipation rates, decreases when T^{Dil} decreases and for increasing α. For each case, the unstable branch of the S-curve progressively vanishes with dilution.

The scalar dissipation rate value under quenching conditions, $\chi_{\mathcal{Z}}^q$, changes according to α and β. Without heat losses (case (a) in Fig. 9), combustion is possible at very high strain rates if dilution is sufficiently high: the increase in reactant temperature induced by mixing with high-enthalpy diluent allows chemical reactions to occur even under high-strain-rate conditions. However, for diluent temperatures below the adiabatic condition, two different scenarios can be identified:
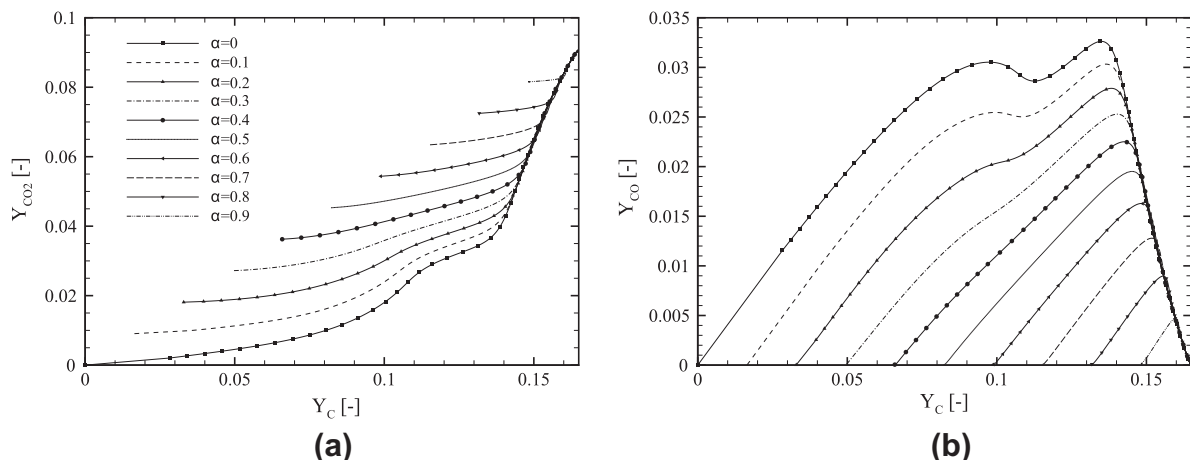
Fig. 7. Profiles of species mass fractions of (a) CO_2 and (b) CO as functions of Y_c; conditions are identical to those used in Fig. 6.
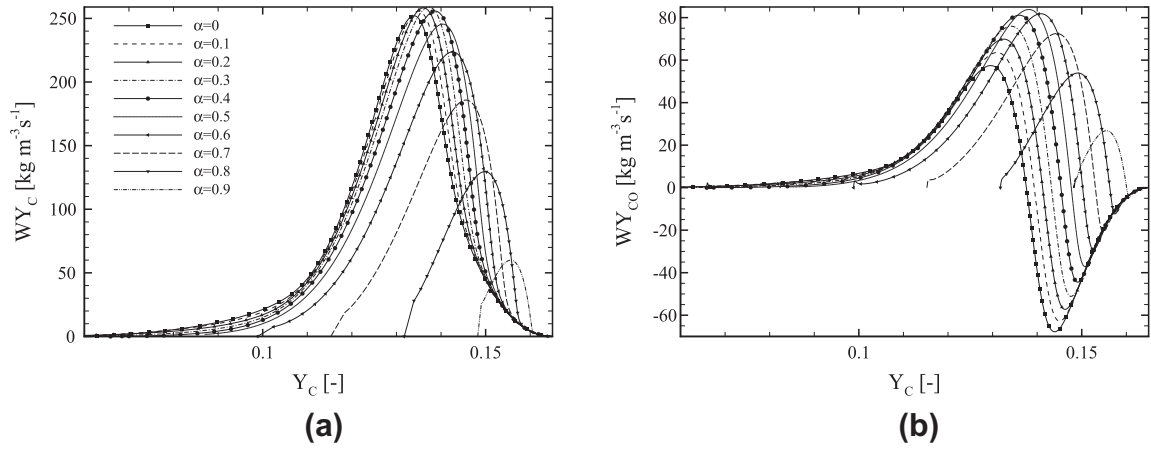
Fig. 8. Profiles of species source terms of (a) Y_c and (b) CO as function of Y_c; conditions are identical to those used in Fig. 6.
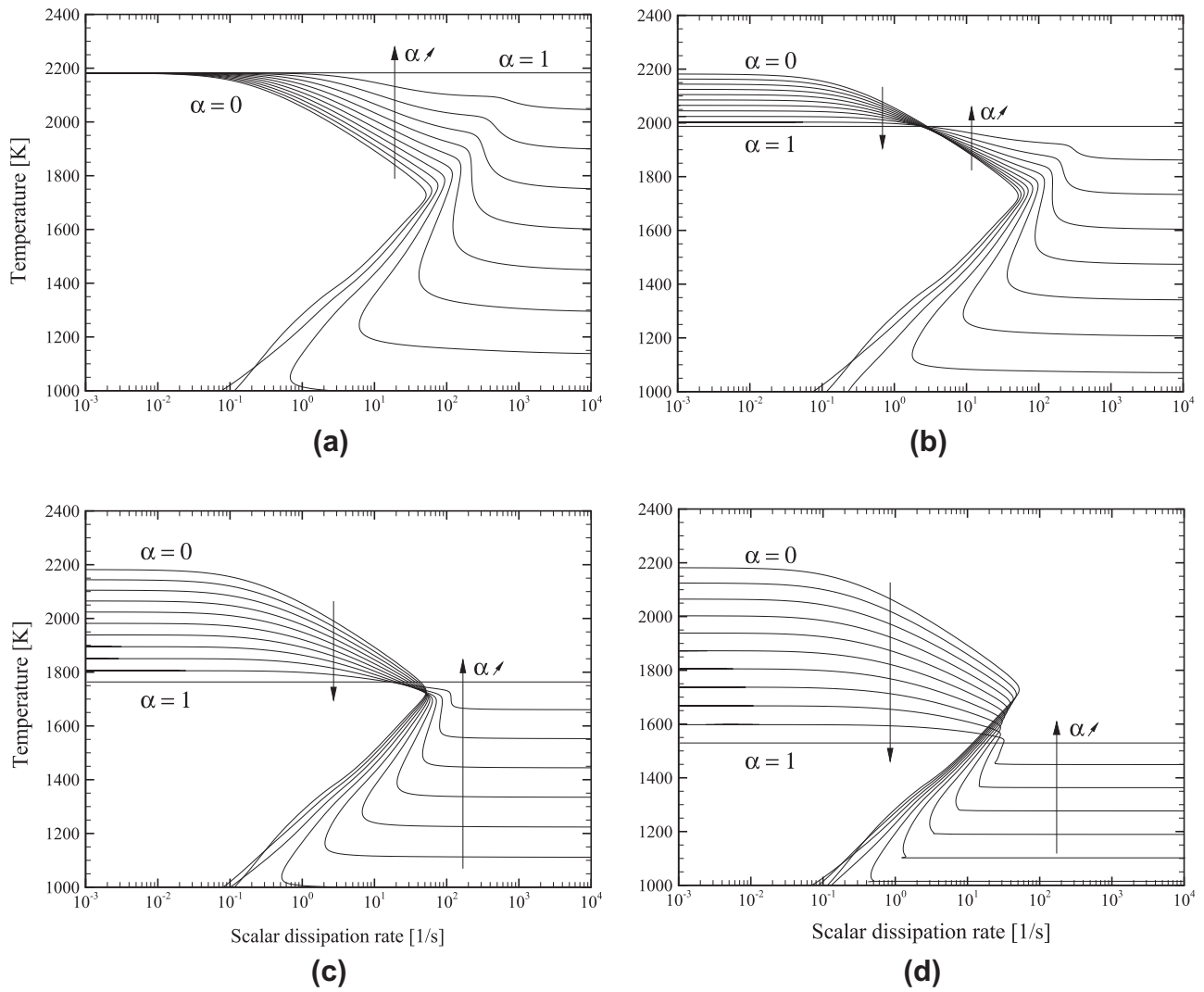

Fig. 9. Steady flamelet temperatures for $\mathcal{Z} = \mathcal{Z}_G$ as function of the scalar dissipation rate for various dilution levels, α. Levels of increasing dilution are indicated by the arrow. Global equivalence ratio is equal to 0.77. (a) $T^{\text{Dil}} = T^{\text{Dil}}_{\beta=0} = 2190$ K; (b) $T^{\text{Dil}} = T^{\text{Dil}}_{\beta=0.2} = 1987$ K; (c) $T^{\text{Dil}} = T^{\text{Dil}}_{\beta=0.4} = 1766$ K; (d) $T^{\text{Dil}} = T^{\text{Dil}}_{\beta=0.6} = 1530$ K.

- For low-heat-loss conditions, the trends are similar to the adiabatic dilution case; χ_Z^q increases with dilution, which favors combustion by transferring thermal energy to the system.
- If heat losses exceed a certain threshold, χ_Z^q decreases with increasing dilution level. As result, the stable branch decreases accordingly.

In conclusion, the establishment of a MILD combustion regime is dependent not only on the dilution with burned reaction products but also on heat losses. While a pronounced dilution of reactants is necessary to achieve MILD combustion, heat losses are of paramount importance in affecting the flame behavior and in extending the stability range in confined combustors with internal recirculation.

3. Turbulent combustion model

3.1. Presumed probability density function model

A statistical description is used to represent the turbulence/chemistry interactions at the sub-grid-scale level. A presumed probability density function (PDF) approach is considered, in which the filtered scalar quantities are written as

$$\widetilde{\psi} = \iiiint \mathcal{G}_\psi(Z, \Lambda, \alpha, \beta) \widetilde{P}(Z, \Lambda, \alpha, \beta) dZ d\Lambda d\alpha d\beta \tag{28}$$

and the density-weighted joint PDF $\widetilde{P}$ is expressed as

$$\widetilde{P}(Z, \Lambda, \alpha, \beta) = \frac{\rho}{\bar{\rho}} P(Z, \Lambda, \alpha, \beta), \tag{29}$$

with P being the nonweighted joint probability density function. The progress parameter Λ is defined to be statistically independent of the mixture fraction Z [31]. By assuming statistical independence of α and β, the joint PDF can then be expressed in terms of marginal distributions:

$$\widetilde{P}(Z, \Lambda, \alpha, \beta) = \widetilde{P}(Z) P(\Lambda) P(\alpha) P(\beta). \tag{30}$$

In the following, a beta-PDF is used to model the mixture fraction distribution, implemented following the approach of Lien et al. [32]. In MILD or highly diluted combustion regimes, the reaction zone is spatially distributed, which is the reason why it was often compared to well-stirred reactors [33,34]. As such, the distributions of the reaction progress, dilution, and heat-loss variables are represented by Dirac functions. After Λ is replaced by the progress variable Y_c, the following thermochemical state-space representation is obtained for the DFPV model:

$$\widetilde{\psi} = \widetilde{\mathcal{D}}_\psi(\widetilde{Z}, S_Z, \widetilde{Y}_c, \bar{\alpha}, \bar{\beta}). \tag{31}$$

Eq. (31) is used to provide information about all Favre-filtered thermo-viscous-chemical quantities (for example, temperature, species, source terms, density, and transport properties). It is noted that by introducing Dirac distributions for the dilution and the heat loss parameters, we can simplify the notation and now write $\bar{\alpha} = \alpha$ and $\bar{\beta} = \beta$.

3.2. Filtered transport equations

In addition to the solution of the conservation equations for mass and momentum, five additional transport equations are required to close the system of equations in the DFPV model. Here, scalar subgrid fluxes are modeled by introducing turbulent diffusivities $D_{T,\psi}$, which are evaluated using a procedure for the dynamic evaluation of the turbulent Schmidt numbers following the method of Lilly [35].

Transport equations for the first two moments of mixture fraction, progress variable, and enthalpy are written as

$$\frac{\partial \bar{\rho} \widetilde{Z}}{\partial t} + \nabla \cdot (\bar{\rho} \tilde{\boldsymbol{u}} \widetilde{Z}) = \nabla \cdot \left(\bar{\rho} (D + D_{T,\widetilde{Z}}) \nabla \widetilde{Z} \right), \tag{32}$$

$$\frac{\partial \bar{\rho} \widetilde{Z''^2}}{\partial t} + \nabla \cdot (\bar{\rho} \tilde{\boldsymbol{u}} \widetilde{Z''^2}) = \nabla \cdot \left(\bar{\rho} (D + D_{T,\widetilde{Z''^2}}) \nabla \widetilde{Z''^2} \right)$$
$$+ 2\bar{\rho} D_T \mid \nabla \widetilde{Z} \mid^2 - \overline{s_{\chi_Z}}, \tag{33}$$

$$\frac{\partial \bar{\rho} \widetilde{Y}_c}{\partial t} + \nabla \cdot (\bar{\rho} \tilde{\boldsymbol{u}} \widetilde{Y}_c) = \nabla \cdot \left(\bar{\rho} (D + D_{T,\widetilde{Y}_c}) \nabla \widetilde{Y}_c \right) + \bar{\rho} \widetilde{\omega}_{Y_c}, \tag{34}$$

$$\frac{\partial \bar{\rho} \widetilde{Y}_d}{\partial t} + \nabla \cdot (\bar{\rho} \tilde{\boldsymbol{u}} \widetilde{Y}_d) = \nabla \cdot \left(\bar{\rho} (D + D_{T,\widetilde{Y}_d}) \nabla \widetilde{Y}_d \right) + \bar{\rho} \widetilde{\omega}_d, \tag{35}$$

$$\frac{\partial \bar{\rho} \widetilde{H}}{\partial t} + \nabla \cdot (\bar{\rho} \tilde{\boldsymbol{u}} \widetilde{H}) = \nabla \cdot \left(\bar{\rho} (D + D_{T,\widetilde{H}}) \nabla \widetilde{H} \right). \tag{36}$$

The mixture-fraction subgrid scalar dissipation rate is modeled using a linear relaxation assumption

$$\overline{s_{\chi_Z}} = 2\bar{\rho} C_\chi D_T \frac{\widetilde{Z''^2}}{\Delta^2}, \tag{37}$$

in which Δ is the LES filter size and C_χ is a model constant taken as unity. Radiation effects in the enthalpy equation are neglected and only convective heat losses to the combustor wall are considered.

To solve the balance equation for the dilution variable (35), the source term $\widetilde{\omega}_d$ needs to be modeled. This term accounts for internal exchange of reaction products from the compositional stream to the dilution stream. Since this requires the consideration of multispecies interaction, this term cannot be analytically related. Therefore, an empirical model for this transfer term is proposed. The role of the source term is to transform burnt gases into diluent. The source term peaks at the condition corresponding to the global equivalence ratio. Whether or not the incoming streams will become diluted then depends on the convective velocity and the diffusivity. For this, we assume that burnt products are instantaneously transformed into the diluent stream in the burnt gas regions. Mathematically, this term is then written as

$$\widetilde{\omega}_d = \underbrace{\frac{1}{\tau}}_{\text{I}} \underbrace{\left(\widetilde{Y}_d^{Dil} - \widetilde{Y}_d \right)}_{\text{II}} \underbrace{\exp \left\{ -\left(\frac{\widetilde{Z} - \mathcal{Z}_G}{\sigma} \right)^2 \right\}}_{\text{III}} \underbrace{\mathcal{H}(C-1)}_{\text{IV}}. \tag{38}$$

This expression consists of four terms that represent the following physical processes:

- **Term I**: This term is the inverse of the time needed to produce diluents, which is here evaluated as $\tau = \Delta t$, assuming instantaneous transfer of products into the dilution stream.
- **Term II**: This term relaxes $\widetilde{Y}_d$ toward its equilibrium value. Y_d^{Dil} is dependent on $\mathcal{Z}$ and corresponds to the value of the product gas composition at equilibrium. Since Y_d is linearly dependent on $\mathcal{Z}$, it can be shown that Y_d^{Dil} is given by:

$$\widetilde{Y}_d^{Dil} = \begin{cases} \frac{\widetilde{Z}}{\mathcal{Z}_G} Y_d|_{\alpha=1} & \text{for } \widetilde{Z} \leqslant \mathcal{Z}_G, \\ Y_d|_{\alpha=1} - \frac{\widetilde{Z} - \mathcal{Z}_G}{1 - \mathcal{Z}_G} Y_d|_{\alpha=1} & \text{for } \widetilde{Z} > \mathcal{Z}_G. \end{cases} \tag{39}$$

- **Term III**: The assumptions made earlier state that the diluent mixture is composed of burnt gases that correspond to the product mixture at the global equivalence ratio. The Gaussian function included here, centered at $\mathcal{Z}_G$, localizes the production of diluent in mixture fraction space and the value for its standard deviation was chosen to be equal to $\sigma = 0.05$.
- **Term IV**: $\mathcal{H}(C-1)$ is the Heaviside function on C. The introduction of this function makes it possible to form diluents only in the fully burned gas mixture.

With the solution of Eqs. (32)–(34), the DFPV-state-variables can then be evaluated as follows:

$$\alpha = \frac{\widetilde{Y}_d}{\widetilde{Y}_d|_{\alpha=1}}, \tag{40}$$

$$\widetilde{Z} = \frac{\widetilde{\mathcal{Z}} - \alpha \mathcal{Z}_G}{1 - \alpha}, \tag{41}$$

$$S_Z = \frac{\widetilde{Z''^2}}{\widetilde{Z}(1 - \widetilde{Z})} = \frac{\widetilde{\mathcal{Z}''^2}}{(\widetilde{\mathcal{Z}} - \mathcal{Z}_G)(1 - \alpha + \alpha \mathcal{Z}_G - \widetilde{\mathcal{Z}})}, \tag{42}$$

$$\beta = \frac{\widetilde{H} - (H_{\alpha=0}^F - H_{\alpha=0}^{Ox})(\widetilde{\mathcal{Z}} - \alpha \mathcal{Z}_G) - (1-\alpha)H_{\alpha=0}^{Ox} - \alpha H^{Dil}|_{\beta=0}}{\alpha(H^{Dil}|_{\beta=1} - H^{Dil}|_{\beta=0})}. \tag{43}$$

4. Application to adiabatic MILD operating regime

To examine the performances of the DFPV model in application to an adiabatic MILD combustion regime, large eddy simulations of a well-insulated combustion chamber are performed. The experimental configuration under consideration has been investigated by Castela et al. [25]. The choice of using LES was motivated by previous investigations by Graça et al. [36], in which it was concluded that RANS computations, associated with EDC or transported PDF combustion models, provide an inadequate description of the scalar mixing processes up to half the length of the combustion chamber.

In this investigation, we will compare the following three combustion models:

- The laminar flamelet model (LFM) of Peters [18], for which only the stable branch of the S-curve is tabulated, and extinction due to quenching is not captured.
- The FPV approach [22], which considers the solution of the unstable branch, but does not account for variations in the reactant composition.
- The DFPV model without heat losses ($\beta = 0$) proposed here.

4.1. Experimental configuration

The configuration is a reversed-flow combustion chamber, in which inlet and exhaust ports are located on the same side. This configuration ensures sufficiently large residence times to complete combustion and to promote intense mixing of burned gases with the unburned reactant stream [37]. Similar reverse-flow configurations have previously been considered [11,12] in order to achieve MILD combustion conditions.

The configuration consists of a cylindrical combustion chamber of 340 mm length and 100 mm diameter. The injection system is composed of a central fuel nozzle with a diameter of 4 mm, supplying natural gas in the volumetric composition ratio $CH_4/C_2H_6/C_3H_8/N_2 = 85.1/7.6/1.9/5.4\%$. Preheated air at 600 K is supplied through an annualar injector with an inner diameter of 14 mm and an outer diameter of 18.5 mm. The exhaust port is an annulus, having an inner diameter of 75 mm and an outer diameter of 90 mm. A schematic of this configuration is shown in Fig. 10.

The operating conditions investigated here are summarized in Table 1. The adiabatic operating condition was indirectly confirmed by comparing computed adiabatic flame-temperature results (at the global equivalence ratio) with reported exhaust temperature measurements, indicating that the measurements are within 5% of the theoretical results. We thus considered that the configuration was adiabatic.

4.2. Computational setup

The finite-volume code YALES2 [38,39] was used to simulate the combustor configuration. In this solver, the Navier–Stokes equations are solved under a low-Mach approximation using a projection method [40] for variable density flows. For the presented computations, the equations are solved in conservative form. A fourth-order finite-volume scheme is used to discretize the spatial operators and a fourth-order Runge–Kutta-type scheme is used for time advancement.

To investigate the sensitivity to the LES mesh resolution, simulations on three different computational grids were performed, and the mesh characteristics are summarized in Table 2.

A detailed analysis of mean-flow results showed that species and temperature statistics were not further improved when the mesh resolution was increased from the medium to the fine grid (Fig. 11). Therefore, only results from the medium mesh are presented.

The lookup table was discretized with $201 \times 15 \times 201 \times 11$ grid points in the direction $\widetilde{Z} \times S_Z \times \overline{C} \times \bar{\alpha}$. The generation of the filtered chemistry table was achieved in approximately 2 h on 12 processors.

Inflow conditions for the oxidizer stream were prescribed from a turbulent velocity profile with 5% turbulent intensity. An analysis of sensitivity to the turbulent intensity was carried out, and negligible impact on the flow field was observed. As for the progress variable, the boundary conditions values associated with the dilution variable are set to zero for every inlet.

4.3. Instantaneous flow field

A comparison of instantaneous temperature field, obtained from all three models is shown in Fig. 12. These qualitative results show that the instantaneous temperature field, predicted by LFM, shows considerably higher temperatures than obtained from the other two models. The maximum temperature is close to the adiabatic temperature of 2150 K. This is due to the model formulation, which does not consider flame extinction (only the upper stable branch of the S-curve is considered). This is further illustrated by showing scatter plots of temperature on a longitudinal cut in Fig. 13 (left). Since this model does not account for extinction events, all reactants mix and burn, and eventually relax toward the equilibrium composition. Combustion is therefore considered to be fast.
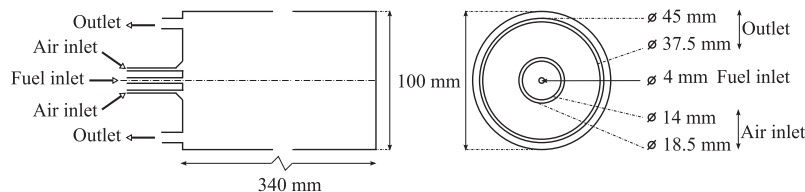
Fig. 10. Schematic view of the combustion chamber geometry of Graça et al. [36], showing (left) a longitudinal cut and (right) a combustor cross-sectional view.

Table 1
Global equivalence ratio ϕ_G, inlet velocity of air- and fuel streams, U_{air} and U_{fuel}, respectively.

ϕ_G	U_{air} (m/s)	U_{fuel} (m/s)	Re_{air}	Re_{fuel}	τ_G^{res} (s)
0.416	108	17, 7	8751	4514	0.211

Note: Reynolds number based on air injector Re_{air} and fuel injector Re_{fuel}, and global residence time τ_G^{res} evaluated as the ratio of the volume of the chamber to the total reactant volume flow rate.

Table 2
Mesh information for the simulation of the configuration of Castela et al. [25].

Mesh	Δ_0 (mm)	DoF	Elements
Coarse	0.4	1.2M	6M
Medium	0.22	5.5M	28.5M
Fine	0.11	41M	228M

Note: Δ_0 denotes the minimum filter size and DoF is degrees of freedom (in millions).

The FPV approach allows for the presence of unburned mixtures as solutions of the flamelet equations (Fig. 12 (middle)). In the present case, the reactant gas temperature at the inlet is too low to promote autoignition. Partial premixing of reactants occurs after injection into the combustion chamber. Reactants are then diluted by recirculating hot burned gases, so that the flame stabilization and combustion are facilitated by diffusion transfer of heat and radical species to the partially premixed reactant mixture. The FPV model predicts a maximum temperature that is considerably lower than the LFM model. This is further illustrated by scatter plots in Fig. 13 (middle). Because of the partial premixing of the reactants, occurring prior to combustion, chemical trajectories converge to the equilibrium condition at $\mathcal{Z} = \mathcal{Z}_G$, thereby bypassing the high-temperature regions around the stoichiometric condition. It is noteworthy to point out that the FPV model predicts combustion of fuel-rich pockets, resulting in the formation of hot spots with temperatures around 1550 K; these spots are shown by the red areas in Fig. 12 (middle).

An instantaneous temperature field predicted by the DFPV model is illustrated in Fig. 12 (right), exhibiting qualitative similarities to the temperature field that is predicted by the FPV model (Fig. 12 (middle)). The detachment of the reaction zone from the region between air and fuel inlets and temperature field is considerably lower than that obtained from the other two simulations. Figure 13 (right) shows that for the whole mixture fraction range, unburned gas states exist. Moreover, the penetration length of the reactants is lower in the DFPV model than in the FPV model, which highlights the effect of dilution on the combustion process.

4.4. Statistical flow field results

A comparison of time-averaged temperature profiles along the combustor centerline is shown in Fig. 14. The temperature predicted by the LFM model is overestimated until 170 mm. The FPV
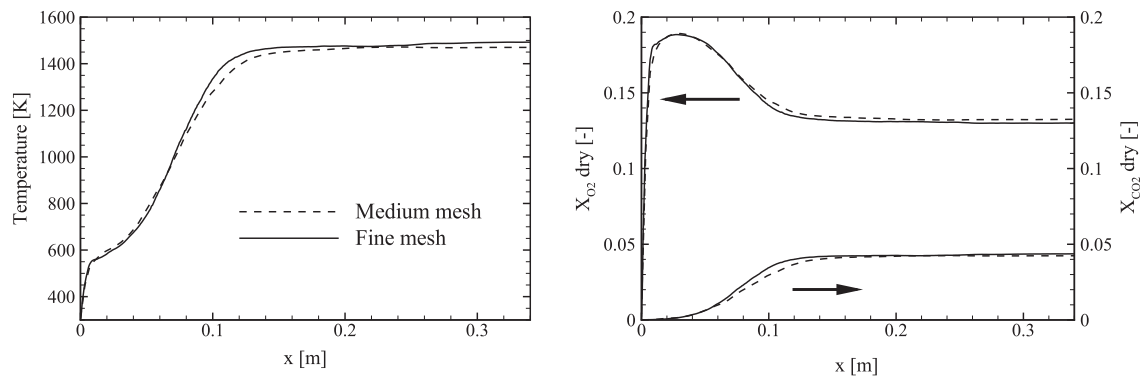

Fig. 11. Mean temperature and dry mole fractions of CO_2 and O_2 along the centerline of the configuration for the medium and fine meshes.
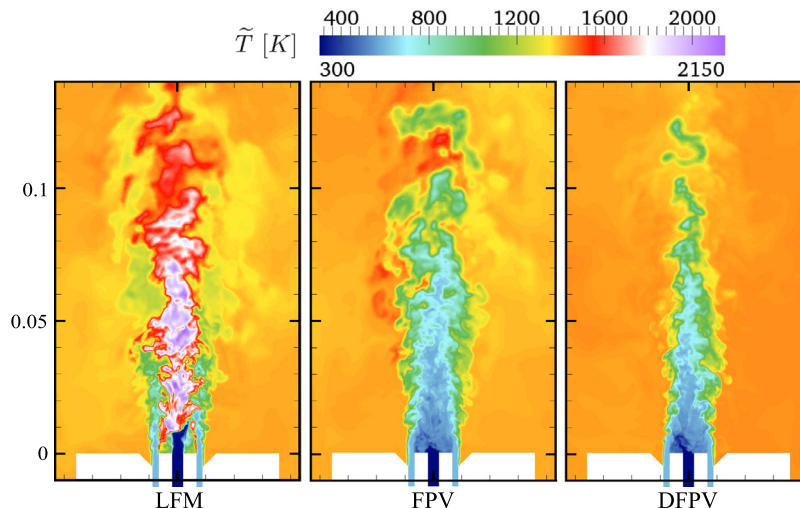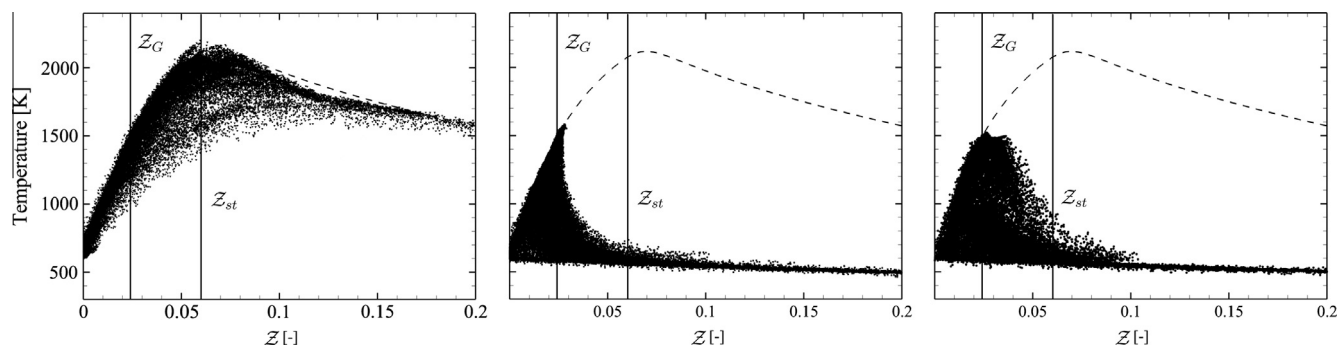

Fig. 12. Temperature fields in a median plane for the three models. The distribution is shown close to the injection system and the spatial scale is given in meters. Left: LFM model; Middle: FPV model; Right: DFPV model.

Fig. 13. Scatterplots of temperature. The solution of an undiluted steady flamelet for $\chi_{st} = 20\,\mathrm{s}^{-1}$ is shown by the dashed line. Left: LFM model; Middle: FPV model; Right: DFPV model.
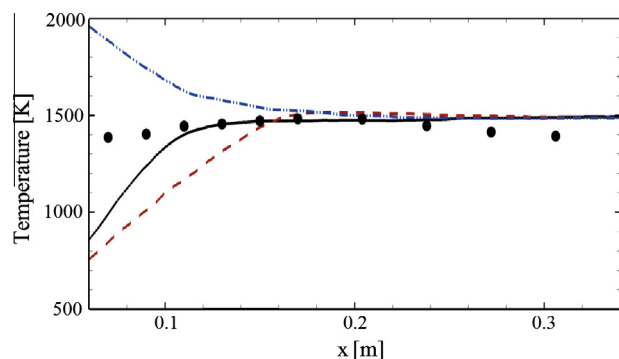
Fig. 14. Time-averaged temperature along the centerline of the configuration. *Symbols*: experimental data points; *Continuous line*: DFPV model; *Dashed line*: FPV model; *Dashed-dot-dot line*: LFM model.

model predicts a lower heat release in the nozzle-near region, and good agreement with experimental data is obtained for $x > 150$ mm, corresponding to 44% of the total length of the combustion chamber. A noticeable improvement is obtained with the DFPV model, where the temperature homogeneity is better reproduced. It is still unclear why discrepancies arise in the nozzle-near region, but it can be speculated that the mixing process requires more precision, because of measurement uncertainties. Moreover, it is noteworthy that the discrepancies appearing in the nozzle-near region are significantly lower than in the RANS computations of Graça et al. [36], where the temperature at the centerline at $x = 70$ mm is overestimated by 800 K.

Similar trends are observed for dry mole fractions of O_2 and CO_2 (shown in Fig. 15). Considerable discrepancies can be observed for

the predictions with the LFM model, while good agreement is obtained for the simulations using the FPV and the DFPV models. This provides further support that the predicted flame characteristics near the injector are representative for this burner configuration.

Comparisons of carbon monoxide mole fractions along the centerline are shown in Fig. 16. Large differences are observed between the three model predictions. The LFM model overpredicts the reaction progress for all equivalence ratios, which leads to a rapid increase of CO in the nozzle-near region. This is followed by a rapid consumption of CO due to the relaxation towards equilibrium. The delayed combustion process predicted by the FPV model yields an overprediction of CO. In contrast, when the dilution of reactants is considered, the model qualitatively captures the trend and the magnitude of the CO profiles.

The accurate prediction of CO is particularly challenging, which is due to its sensitivity to the reaction chemistry and local flow-field composition. The following comparison of CO results emphasizes the importance of considering dilution effects in the combustion model. To illustrate the formation and consumption of CO inside the combustor, we evaluate scatter data in CO–CO_2 composition space throughout the combustor. These results are presented in Fig. 17, confirming that dilution has a considerable influence on the CO conversion. When dilution effects are neglected, the only trajectory available is defined by the undiluted case, and the production of CO is unsatisfactory. The results obtained from this large eddy simulation substantiate the laminar flame investigations and show that the flame structure and minor-species conversion exhibit pronounced sensitivity to the dilution of the reactant gases. Furthermore, these simulations demonstrate the capability of the proposed DFPV model in predicting internal dilution systems and dilution-controlled MILD combustion.
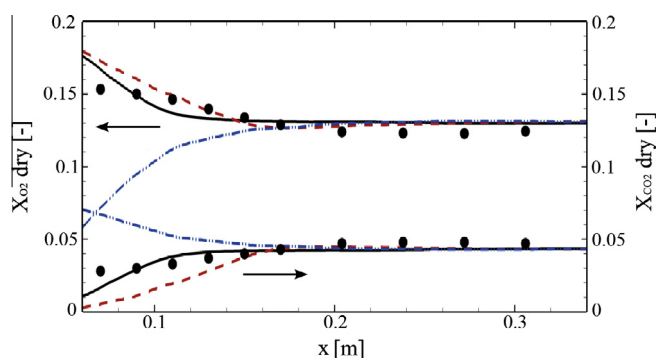
Fig. 15. Comparisons of temporally averaged centerline profiles for mole fractions of O_2 and dry CO_2. *Symbols*: experimental data points; *Continuous line*: DFPV model; *Dashed line*: FPV model; *Dashed-dot-dot line*: LFM model.
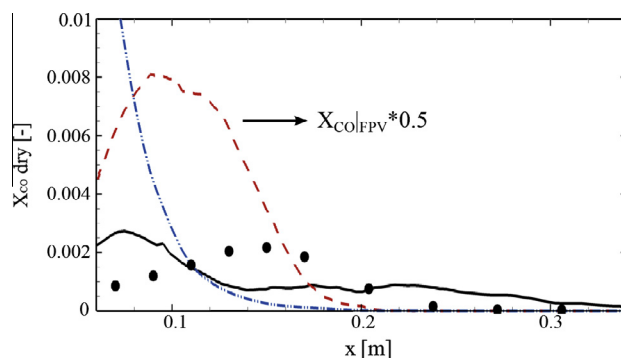
Fig. 16. Comparisons of temporally averaged centerline profile for dry mole fractions of CO. *Symbols*: experimental data points; *Continuous line*: DFPV model; *Dashed line*: FPV model; *Dashed-dot-dot line*: LFM model.
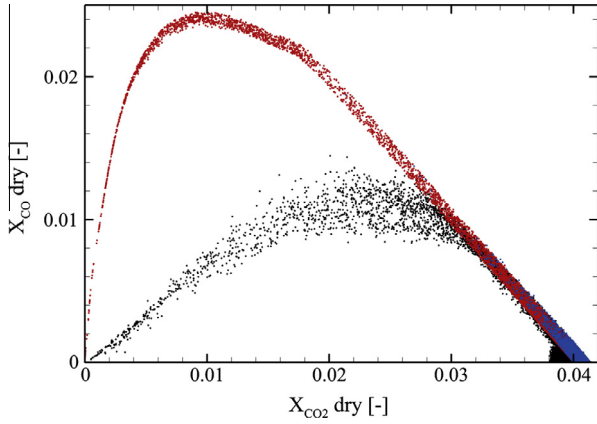
Fig. 17. Scatterplots of CO as a function of CO_2 (in dry mole fractions) for $\widetilde{Z} = \mathcal{Z}_G \pm 0.002$. *Black*: DFPV; *Red*: FPV; *Blue*: LFM.

Fig. 18. Percentage of volume occupied by cells conditioned by the flame index GI_Z.

4.5. Flame structures analysis

The Takeno index [41] is used to discriminate combustion modes in the combustion chamber. Yet the formulation of this index poses issues when detailed chemistry effects are taken into account and in the absence of reactants. To overcome these deficiencies, another flame index is proposed.

As mentioned in several studies [42–44], in moderately curved diffusion flames, the gradients of Z ($\hat{\boldsymbol{n}}_Z = \nabla Z / |\nabla Z|$) and Y_c ($\hat{\boldsymbol{n}}_{Y_c} = \nabla Y_c / |\nabla Y_c|$) are aligned so that $\hat{\boldsymbol{n}}_Z \cdot \hat{\boldsymbol{n}}_{Y_c} \pm 1$. For weakly stratified flames and premixed flames that are subjected to low strain, the flame front is perpendicular to iso surfaces of mixture fraction, which implies that $\hat{\boldsymbol{n}}_Z \cdot \hat{\boldsymbol{n}}_{Y_c} = 0$. In partially premixed combustion, one can then obtain $-1 < \hat{\boldsymbol{n}}_Z \cdot \hat{\boldsymbol{n}}_{Y_c} < 1$. In the following, we define the flame index GI_Z as:

$$GI_Z = \frac{\nabla \widetilde{Z} \cdot \nabla \widetilde{Y}_c}{|\nabla \widetilde{Z}| |\nabla \widetilde{Y}_c|} \bigg|_{\widetilde{\dot{\omega}}_C > \epsilon}. \tag{44}$$

To ensure that we analyze only the reaction zone, this index is conditioned on the source term of the reaction progress variable and ϵ is a parameter, which is here chosen to be equal to 1 s^{-1}. $GI_Z = \pm 1$ defines a diffusion-controlled combustion mode. It is important to note that Eq. (44) does not account for subgrid contributions. To assess the significance of subgrid contributions, we evaluated the flame index for the medium and the fine mesh, and both provide quantitatively similar results. The flame index is computed from resolved quantities. It is expected that the qualitative nature of the predicted flame structure is weakly sensitive to the errors induced by the turbulent combustion model, even if a feedback on the resolved quantities is expected. On tetrahedra-based meshes with high variations in the cell size, the distribution of GI_Z needs to be weighted by cell volumes to estimate the volumetric contribution of the different combustion modes that are present inside the burner. The discrete volume-weighted flame index is written as

$$\zeta_Z = \frac{\sum V_{\text{cell}}|_{\widetilde{\dot{\omega}}_C > \epsilon; GI_Z}}{\sum V_{\text{cell}}|_{\widetilde{\dot{\omega}}_C > \epsilon}} \tag{45}$$

The distribution of the volume-weighted flame index is illustrated in Fig. 18. The distribution exhibits a bimodal shape, indicating that combustion mainly occurs in the diffusion-controlled regime. A quantitative analysis showed that more than 55% of the reaction zone volume is characterized by $\widetilde{Z}$–$\widetilde{Y}_C$ alignment angles in the range of $[-\pi/6, \pi/6]$ or $[-5\pi/6, 5\pi/6]$ radians.
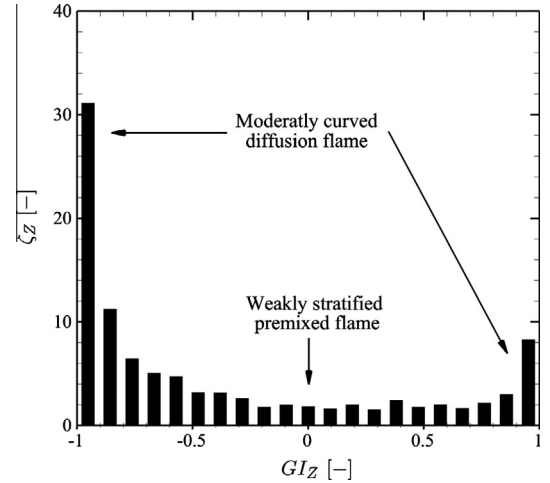
These results allow us to conclude that the combustion in this reverse-flow combustor is primarily dominated by nonpremixed combustion. However, a nonnegligible contribution to the reaction occurs in gas pockets where GI_Z differs from ± 1, indicating the presence of premixed and partially premixed combustion regimes. This implies that the DFPV model is able to represent these flame topologies at strongly diluted MILD combustion regimes.

5. Application to a nonadiabatic MILD operating regime under consideration of wall heat-loss effects

In the previous section, the applicability of the DFPV model for the prediction of dilution-controlled combustion regimes without consideration of heat-loss effects was examined. However, in practical applications, heat losses play an important role in affecting the combustion stability and species distribution. The performances of several models with different degree of complexity are here evaluated in application to a nonadiabatic configuration:

- The FPV approach [22], which does not account for variations in reactant composition and heat-losses. Note that the LFM model predictions are here omitted as they collapse on the FPV approach estimations.
- A simplified DFPV approach, denoted "sDPFV," where dilution and heat losses are correlated in time and space. This approach implies a unique value of the dilution ratio α for a given enthalpy defect. This model is derived from the DFPV formulation, and modeling details are presented in Appendix A.
- The proposed DFPV model allows for compositional variations as well as heat-loss effects without enforced correlations.

5.1. Experimental configuration

A schematic of the confined combustor configuration is presented in Fig. 19. This burner was experimentally studied by Verissimo et al. [16]. The cylindrical combustor has a diameter of 50 mm and a length of 50 mm. The reaction products exit through a convergent nozzle of length 150 mm and 15 degrees. Preheated air at 673 K is injected through a central nozzle, having a diameter of 10 mm. Methane fuel under ambient conditions is supplied through 16 separated nozzle holes (2 mm in diameter), which are coaxially located at a radius of 15 mm. The fuel inlet velocity is fixed at 6.2 m/s, and the experimental investigations consider only
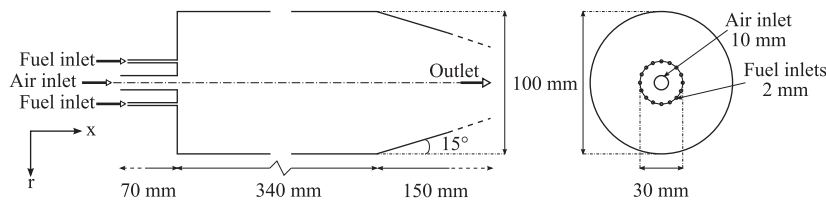
Fig. 19. Schematic view of the combustion chamber geometry of Verissimo et al. [16] through a longitudinal cut (left), and a cross-sectional cut through the burner (right).

Table 3
Global equivalence ratio ϕ_G, air inlet velocities U_{air}, Reynolds number based on air injector Re_{air} and global residence time τ_G^{res}.

Run	ϕ_G	U_{air} (m/s)	Re_{air}	τ_G^{res} (s)
2	0.77	113.2	17,526	0.29
4	0.58	143	22,140	0.23

variations in the air mass flow rate, thereby changing the overall equivalence ratio.

In the following, two operating conditions are considered, namely "run 2" and "run 4." The corresponding operating conditions are summarized in Table 3. As reported in the experimental study, high-momentum air injection increases the recirculation and the mixing of unburned reactants with reaction products. This results in a homogeneous temperature field and ultralow emissions of CO and NO$_x$. Verissimo et al. [16] studied the effect of excess air on the combustion regime and reported a gradual deviation from MILD combustion when the excess air coefficient was increased. Probe measurements were conducted to determine species concentrations and the temperature field inside the combustor. From the measurements, it was concluded that with increasing excess air the flame structure shifts from a homogeneous reaction zone toward a recirculating flame that stabilizes in proximity to the fuel injector.

The operating point denoted as "run 4" features the characteristics of a conventional lean combustion process. The authors of the experimental study reported a localized reaction zone and a clearly visible flame front. For the second case (designated "run 2") the measurement indicates that the combustion occurs in the MILD combustion regime: the reaction zone is distributed over a large volume and no flame front is visible. For both operating conditions, CO and NO$_x$ emissions are below 10 ppm. The measurement database includes mean flow results for temperature, O$_2$, CO$_2$, CO, NO$_x$, and unburned hydrocarbons (UHC) along axial and radial sections in the burner. The reported reproducibility of the experimental data is 5% for temperature and approximately 10% for species measurements.

5.2. Computational setup

Simulations with two different grid resolutions have been performed (Table 4). A further grid refinement study was performed but did not show noticeable influence on the scalar mean flow quantities. Therefore, only results obtained with the fine mesh of

Table 4
Mesh information for the simulation of the configuration of Verissimo et al. [16].

Mesh	Δ_0 (mm)	DoF	Elements	N_{air}
Coarse	0.4	2.58M	13.7M	~25
Fine	0.22	8.45M	48.9M	~45

Note: Δ_0 denotes the minimum filter size and DoF is degrees of freedom (in millions); N_{air} is the number of grid points along a diameter of the air inlet.

48.9 million control volumes are presented in the following. The fuel inlet velocity was prescribed by a laminar profile and turbulent inlet conditions were used for the air injection. Turbulent fluctuations with different turbulence levels (Tu$_{inj}$ = 5% for run 4, and Tu$_{inj}$ = 5% or 1% for run 2) have been superposed on the mean flow, which was evaluated from a periodic pipe flow simulation. From this study it was found that the mean velocity profile along the centerline is sensible to the turbulent intensity, but no experimental information about the velocity field was reported to guide the simulation setup.

Figure 20 shows the thermodynamic equilibrium temperature computed for different values of the equivalence ratio. The range of temperatures accessed in the experiments is added in the figure for the ϕ_G = 0.58 and ϕ_G = 0.77 cases. The maximal temperature reached in the experiment is 150 K and 350 K below the equilibrium states for run 4 and run 2, respectively. This comparison implies that in these simulations, the impact of the prescription of the boundary conditions is of importance, since heat losses are significant. Wall temperature measurements were not reported, but the extrapolation of the measured radial temperature profiles from the chamber gives an estimate of the wall temperature in the range of 1200 ± 200 K. Based on this estimate, we prescribed a constant wall temperature of 1200 K for all simulations. By invoking the low temperature of the combustion process and the relatively low global residence times found in the configuration, radiation effects were neglected in the following simulations.

The DFPV table was discretized with $151 \times 15 \times 121 \times 11 \times 11$ grid points in the direction $\widetilde{Z} \times S_Z \times \overline{C} \times \bar{\alpha} \times \bar{\beta}$. The generation of the DFPV table, including the computation of the flamelets, took approximately 5 h on 24 processors.

5.3. Flow field topology

The high momentum of the air stream inlet promotes the generation of a reverse flow, which advects hot burnt gases toward the
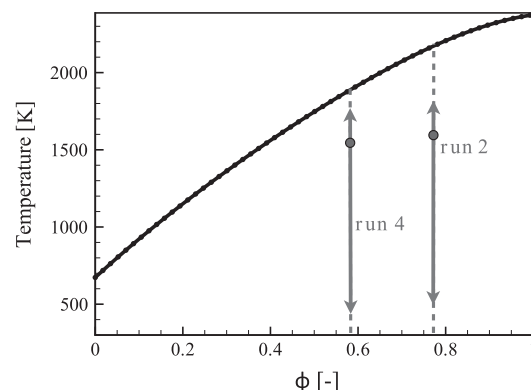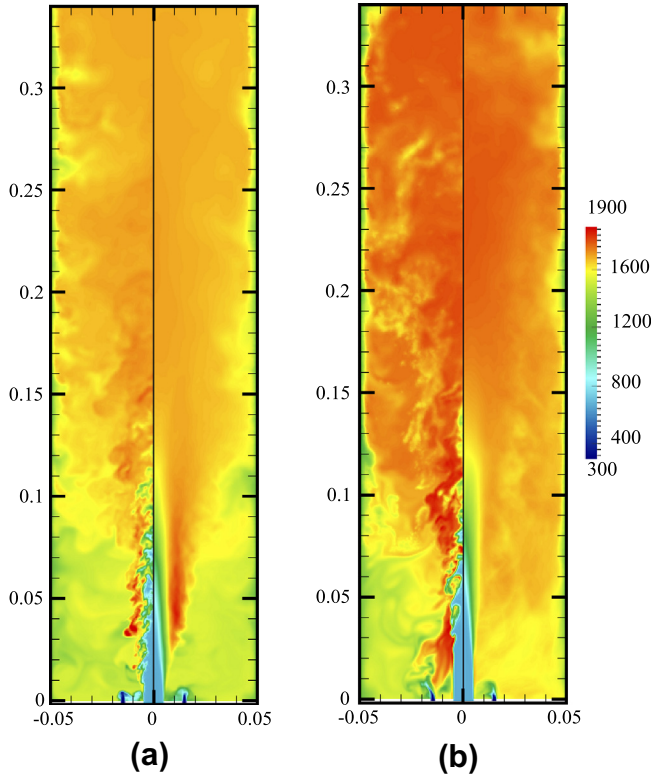

Fig. 20. Thermochemical equilibrium temperature as a function of the mixture equivalence ratio ϕ under Verissimo et al. [16] operating conditions. Arrows represent the range of measured temperature in the experimental data, and symbols indicate the mean temperature at the exit of the combustion chamber.

fresh reactants. The two operating conditions impact directly the diluent composition, which contains large amounts of oxygen for run 4. A comparison of instantaneous temperature fields, obtained under the two operating conditions, is shown in Fig. 21. In both cases, low-velocity regions, 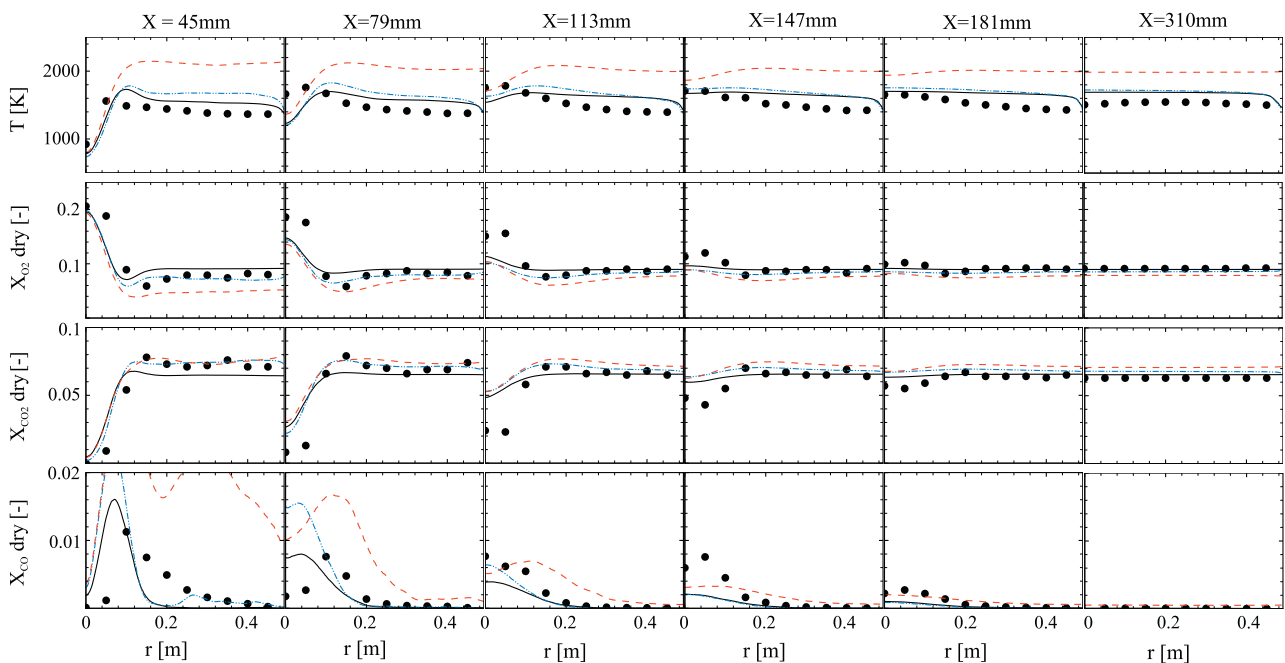localized for $x \in [0, 50]$ mm and $r \in [20, 50]$ mm, exhibit burned gas temperatures lower than at the chamber exit. This is attributed to the heat transfer to the walls and to the long residence times found in these regions. For run 4, a high-mean-temperature region (>800 K) can be located at the interface between the oxidizer stream and burned gases mixed with methane. For run 2, the mean temperature distribution is more homogeneous and the temperature is higher than in run 4 due to its global equivalence ratio, which is closer to stoichiometry. The instantaneous distributions of run 2 present localized and intermittent high-temperature spots (>1900 K). The mean behavior of the two cases is similar to that observed experimentally.

### 5.4. Statistical flow-field results for run 4: $\phi_G = 0.58$

Radial profiles of temperature and dry species mole fractions are given in Fig. 22 for run 4. Experimental results are shown by symbols. The predicted temperature, obtained from the two DFPV approaches, is in good agreement with measurements. The FPV model overestimates the temperature by 400 K throughout the combustion chamber. This shows the importance of heat-loss and dilution effects. Temperature predictions that are obtained from both DFPV models exhibit moderate discrepancies (<100 K) for radial position $r > 5$ mm. By computing unsteady flamelets subject to radiation, comparison between the characteristic radiation time [31] and the global residence time of the configuration showed that temperature overpredictions can be attributed to the neglect of radiation effects.

Predictions of major species mole fractions are in good agreement for all models. Contrary to the temperature distributions, major species are less sensitive to heat losses, which explains the similar results. However, discrepancies can be observed along the centerline of the configuration, for $x \in [45, 113]$ mm and $r \in [0, 5]$ mm. The mole fraction of O_2 is underestimated, while CO_2 is overestimated.

Similarly to the results presented in Section 4, the predictions of carbon monoxide feature very different evolutions depending on the combustion model. In the experimental data, the CO spreads widely in radial direction at the first few probe stations (from 45

Fig. 21. Instantaneous (left) and mean (right) temperature fields in a median plane for the two operating conditions using the DFPV model. Spatial dimensions are in units of meters. (a) Run 4; (b) run 2.

Fig. 22. Comparison of statistical results at different axial locations in the burner for the operating conditions of run 4, showing (from top to bottom) temperature, and dry mole fractions of O_2, CO_2 and CO. *Symbols*: experimental data points; *continuous line*: DFPV model; *dashed-dot-dot line*: sDFPV model; *dashed line*: FPV model.
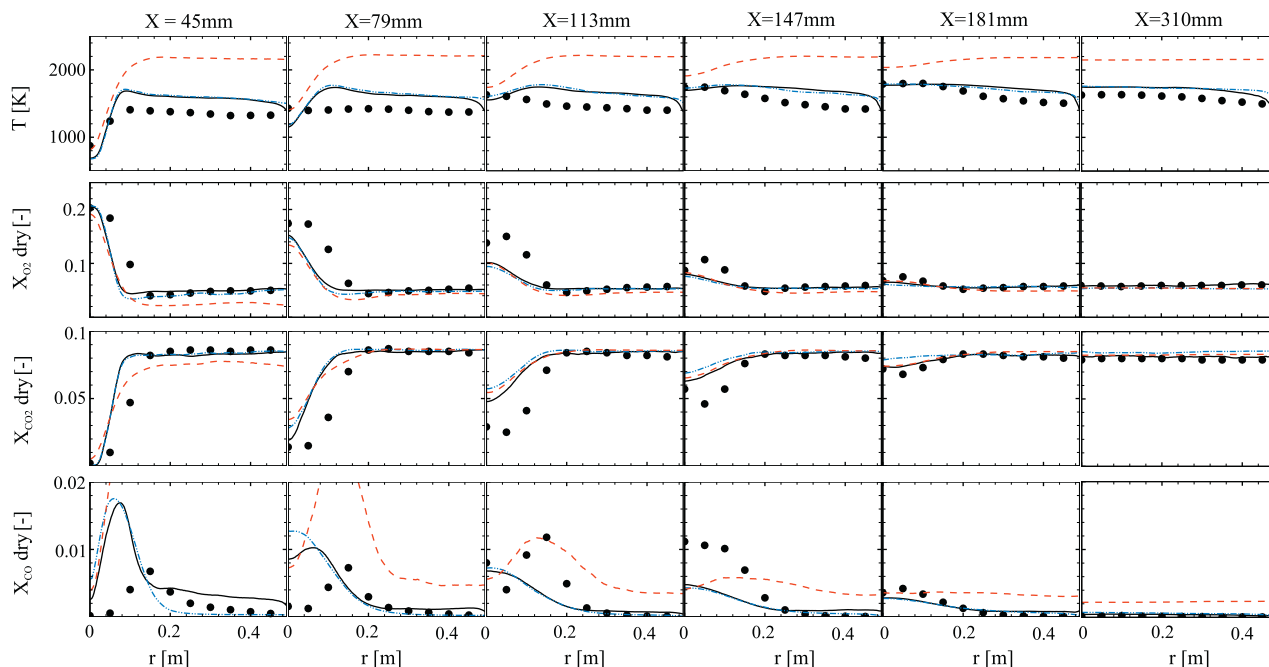
Fig. 23. Comparison of statistical results at different axial locations in the burner for the operating conditions of run 2, showing (from top to bottom) temperature, and dry mole fractions of O_2, CO_2, and CO. _Symbols_: experimental data points; _continuous line_: DFPV model; _dashed-dot-dot line_: sDFPV model; _dashed line_: FPV model.

to 147 mm). The DFPV model is the only model able to reproduce the correct order of magnitude for CO, even if the predictions are not satisfactory from 79 to 147 mm. Yet Fig. 22 provides evidence of the importance of the product gas dissociation and heat losses. More specifically for pollutant emissions, the observed differences between the DFPV models can be attributed to the prescription of the β parameter in the sDFPV model, which implies that several chemical trajectories are not considered (see A.2 for further details).

5.5. Statistical flow-field results for run 2: $\phi_G = 0.77$

Radial profiles of temperature and dry species mole fractions for run 2, corresponding to a MILD combustion regime, are compared with experimental data in Fig. 23. Similarly to run 4, the FPV model without consideration of dilution and heat losses overpredicts temperature and CO profiles. Temperature predictions from the DFPV and the sDFPV models are very similar, and in good agreement with experimental data. It is encouraging to note that both developed models converge toward the same equilibrium (probe stations located at $x \in [181 \text{ mm}; 310 \text{ mm}]$). However, a slight underestimation of temperature is noticeable along the axis of symmetry for regions located between 45 and 79 mm. Away from the core region ($r > 5$ mm), the DFPV models predict higher temperatures than seen in the experiments. Computations of unsteady laminar flamelets subject to radiation for these operating conditions suggest that this might be due to the neglect of radiation. However, these discrepancies might also be sensitive to the prescribed wall temperature, for which no experimental data are available. Yet these models demonstrate their capacity to reproduce heat loss effects.

Predictions for major species are in better agreement. Discrepancies arise in the region $x \in [11, 113]$ mm and $r \in [5, 15]$ mm, for which O_2 is under-predicted and CO_2 is overestimated. A similar discrepancy between temperature and major species was also observed for run 4. These discrepancies may be attributed to the modeling hypothesis on the diluent composition, or to experimental uncertainties. Predictions of CO are consistent with

temperature and major species estimate. The misprediction of the CO mole fraction at the first measurement station can be explained by the sensitivity of CO to the temperature field.

Differences between results from the DFPV and the sDFPV models are very low for these operating conditions. For run 2, the DFPV model relaxes toward the sDFPV approach, indicating that for this specific condition the combustion process is most likely controlled by heat losses rather than dilution effects. Nevertheless, both DFPV approaches are able to adequately reproduce the first moments of species and temperature field for both conventional and MILD combustion regimes.

6. Conclusions

Modeling challenges of MILD combustion arise from the pronounced dilution of reactants, which induces compositional variations. The dilution influences the reaction chemistry and models should therefore be able to account for these effects. Moreover, most practical combustor configurations operate under nonadiabatic conditions, which requires the consideration of wall heat-loss effects to adequately describe the flame stabilization, fuel conversion, and emissions.

In this contribution, a turbulent combustion model was proposed that extends a tabulated chemistry model to account for product gas dilution and heat-loss effects. Simplifying assumptions were formulated to decrease the model complexity. Two tabulation approaches that extend the FPV model were introduced: the DFPV model, where dilution and heat losses may evolve on different spatiotemporal scales, and the sDFPV model, where both phenomena are constrained. To investigate effects of dilution and heat losses on the flame structure, a laminar flame-response analysis was performed. Results from this analysis emphasize the significance of dilution in the nonequilibrium chemistry and flame stabilization.

A turbulent closure model was proposed, using a presumed PDF method to account for turbulence chemistry coupling. An exchange model for transferring reaction products into the dilution stream was formulated. This model was then applied in large eddy

simulations, and two different combustor configurations were considered. In the first case, results obtained with the DFPV model were in good agreement with experimental data. It was shown that the consideration of dilution effects leads to considerable improvements in the CO prediction, demonstrating that the thermochemical trajectory is influenced by dilution. In the second application, a combustor configuration was considered that is operated in the conventional and the MILD operating regime. Overall, the simulation results obtained with the proposed model are in reasonable agreement, demonstrating the ability of the model to capture effects of species dilution and heat losses on the flow-field structure and species composition. Future improvements in the model require the consideration of radiation effects and the generalization of the dilution exchange, which is currently represented by an empirical closure model.

The proposed tabulated chemistry method assumes that the inner structure of the turbulent flame front is close to a laminar flame. This assumption remains to be further investigated for low-temperature flames. Indeed, when the chemical activities slow down, turbulent eddies penetrate the flame front and may affect the chemical trajectories. Modeling this phenomenon is a challenging problem.

Acknowledgments

Appendix A. Simplified DFPV approach with correlated dilution and heat-loss evolution

A.1. Model formulation

A simplified DFPV tabulation approach, similar to the one developed by Abtahizadeh et al. [28], can be obtained by assuming that the temperature of the diluent is fixed (β is therefore assumed constant in the entire combustor). A schematic of this approach is illustrated in Fig. A.1. This assumption constrains heat losses to the dilution rate and implies that both phenomena evolve similarly in space and time. When the diluent temperature is fixed, the reaction chemistry is then tabulated as a function of three parameters:

$$\psi = \mathcal{G}_\psi^\beta(Z, Y_c, \alpha). \tag{A.1}$$

In the following, this model is referred to as the "sDFPV" model. The validity of this simplifying assumption is assessed in an application to a practical configurations in Section 5. In this model, heat losses and dilution effects are linked, so that H^{Dil} is constant and α reduces to

$$\alpha = \frac{H - \mathcal{Z}(H^{\mathrm{F}}_{\alpha=0} - H^{\mathrm{Ox}}_{\alpha=0}) - H^{\mathrm{Ox}}_{\alpha=0}}{H^{\mathrm{Dil}} - \mathcal{Z}_{\mathrm{G}}(H^{\mathrm{F}}_{\alpha=0} - H^{\mathrm{Ox}}_{\alpha=0}) - H^{\mathrm{Ox}}_{\alpha=0}}. \tag{A.2}$$

In the context of LES, the filtered relation for α is directly expressed from Eq. A.2,

$$\alpha = \frac{\widetilde{H} - \widetilde{\mathcal{Z}}(H^{\mathrm{F}}_{\alpha=0} - H^{\mathrm{Ox}}_{\alpha=0}) - H^{\mathrm{Ox}}_{\alpha=0}}{H^{\mathrm{Dil}} - \mathcal{Z}_{\mathrm{G}}(H^{\mathrm{F}}_{\alpha=0} - H^{\mathrm{Ox}}_{\alpha=0}) - H^{\mathrm{Ox}}_{\alpha=0}}, \tag{A.3}$$

and this model requires only information about the enthalpy $\widetilde{H}$ and the mixture fraction $\widetilde{\mathcal{Z}}$.
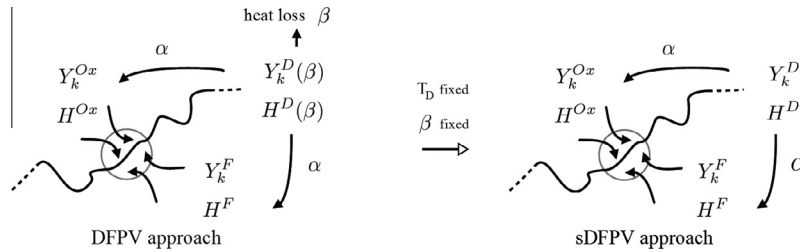
Fig. A.1. Schematic representation of the different constraints imposed on temperature and species of the boundary conditions used to generate counterflow diffusion flames; *left*: DFPV model; *right*: sDFPV model.
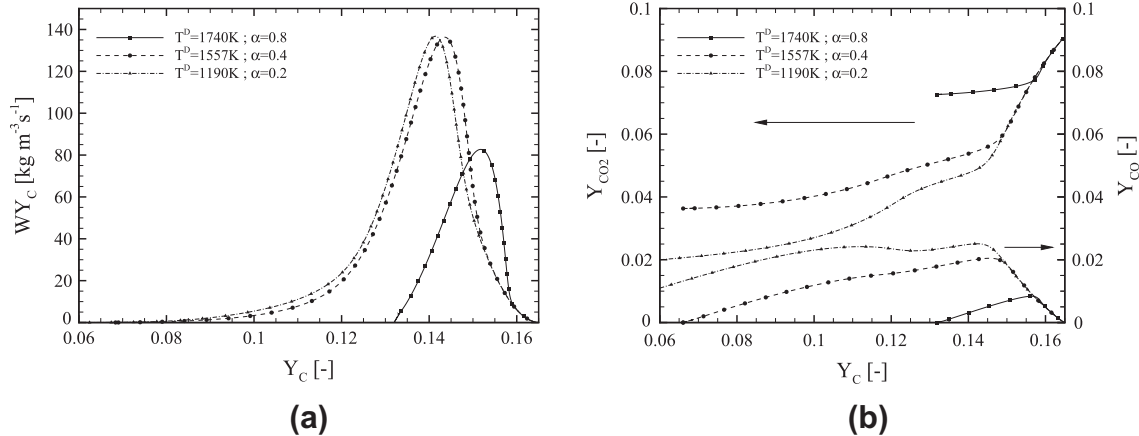
Fig. A.2. Flamelet solutions for $\mathcal{Z} = \mathcal{Z}_{\mathrm{G}}$ ($\phi = 0.58$) and a diluted reactant streams temperature of 1775 K for different values of α and β. For the sake of clarity, only three solutions have been illustrated. (a) Reaction rate of progress variable; (b) CO mass fraction.

A.2. A priori comparison between DFPV and sDFPV models

It is noteworthy that the sDFPV approach depends on the chosen value of β. A preliminary analysis is done to assess the sensitivity of the flame responses when different values of the heat loss parameter are applied. To analyze the importance of neglected trajectories in the sDFPV model, the study of the chemical trajectories giving the same diluted reactant streams temperature is of interest. By prescribing a temperature, at a given equivalence ratio, an iterative sorting procedure can be employed to recover the corresponding (α, β) parameter pair.

In the following, the mixture fraction is fixed to $\mathcal{Z} = \mathcal{Z}_G$ for the run 4 investigated in Section 5.1, and the diluted reactant streams temperature is fixed to 1775 K, which corresponds to the maximal mean temperature obtained in this case. Figure A.2(a) illustrates three solutions of the sorting procedure and presents the reaction rate $\dot{\omega}_{Y_c}$ as a function of Y_c. The DFPV model accounts for all solutions, whereas the sDPFV model allows only for a single trajectory. The strongest reaction zone is shifted toward high values of Y_c for increasing values of the diluent temperature. As these trajectories are strongly dependent on the parameterization (α, β), the reaction zone can consequently be poorly predicted by the sDFPV model if nonequilibrium chemistry effects are important.

The influence of the diluent temperature on species evolutions is highlighted in Fig. A.2(b). Even if the equilibrium mass fractions are very similar, very different trajectories are found. Therefore, the arbitrary prescription of the value of β required in the sDFPV model can have a dramatic influence on the combustion process and pollutant formation.

References

[1] A. Cavaliere, M. de Joannon, Prog. Energy Combust. Sci. 30 (2004) 329–366.
[2] M. Oberlack, R. Arlitta, N. Peters, Combust. Theory Model. 4 (2000) 495–509.
[3] J.A. Wünning, J.G. Wünning, Prog. Energy Combust. Sci. 23 (1997) 81–94.
[4] M. Katsuki, T. Hasegawa, Proc. Combust. Inst. 27 (1998) 3135–3146.
[5] N. Rafidi, W. Blasiak, A.K. Gupta, J. Eng. Gas Turb. Power 130 (2008) 023001.
[6] T. Plessing, N. Peters, J.G. Wunning, Proc. Combust. Inst. 27 (1998) 3197–3204.
[7] W. Yang, W. Blasiak, Int. J. Therm. Sci. 44 (2005) 973–985.
[8] M. Mancini, R. Weber, U. Bollettini, Proc. Combust. Inst. 29 (2002) 1155–1163.
[9] M. Mancini, P. Schweppe, R. Weber, S. Orsino, Combust. Flame 150 (2007) 54–59.
[10] N. Schaffel, M. Mancini, A. Szlek, R. Weber, Combust. Flame 156 (2009) 1771–1784.
[11] S. Kumar, P. Paul, H. Mukunda, Proc. Combust. Inst. 29 (2002) 1131–1137.
[12] G. Szegö, B. Dally, G. Nathan, Combust. Flame 154 (2008) 281–295.
[13] B.B. Dally, A.N. Karpetis, R.S. Barlow, Proc. Combust. Inst. 29 (2002) 1147–1154.
[14] S. Orsino, R. Weber, U. Bollettini, Combust. Sci. Technol. 170 (2001) 1–34.
[15] S. Kumar, P. Paul, H. Mukunda, Combust. Sci. Technol. (2007) 2219–2253.
[16] A.S. Verissimo, A.M.A. Rocha, M. Costa, Energy Fuels 25 (2011) 2469–2480.
[17] G. Smith, D.M. Golden, M. Frenklach, N.W. Moriarty, B. Eiteneer, M. Goldenberg, C.T. Bowman, R.K. Hanson, S. Song, W.C. William, J. Gardiner, V.V. Lissianski, Z. Qin, 1999. <http://www.me.berkeley.edu/gri-mech/>.
[18] N. Peters, Prog. Energy Combust. Sci. 10 (1984) 319–339.
[19] O. Gicquel, Ph.D. thesis, Ecole Centrale Paris, 1999.
[20] J.A. van Oijen, L.P.H. de Goey, Combust. Sci. Technol. 161 (2000) 113–137.
[21] B. Fiorina, R. Baron, O. Gicquel, D. Thevenin, S. Carpentier, N. Darabiha, Combust. Theory Model. 7 (2003) 449–470.
[22] C. Pierce, P. Moin, J. Fluid Mech. 7 (2004) 73–97.
[23] M. Ihme, Y.C. See, Proc. Combust. Inst. 33 (2011) 1309–1317.
[24] M. Ihme, J. Zhang, G. He, B. Dally, Flow Turbul. Combust. (2012) 1–16.
[25] M. Castela, A.S. Verissimo, A.M.A. Rocha, M. Costa, Combust. Sci. Technol. 184 (2012) 243–258.
[26] M. Ihme, C.M. Cha, H. Pitsch, Proc. Combust. Inst. 30 (2005) 793–800.
[27] M. Ihme, L. Shunn, J. Zhang, J. Comput. Phys. 231 (2012) 7715–7721.
[28] E. Abtahizadeh, J. van Oijen, P. de Goey, Combust. Flame 159 (2012) 2155–2165.
[29] R.W. Bilger, S.H. Starner, R.J. Kee, Combust. Flame 80 (1990) 135–149.
[30] H. Pitsch, 1998. <http://www.itv.rwth-aachen.de/downloads/flamemaster/>.
[31] M. Ihme, H. Pitsch, Phys. Fluids 20 (2008) 055110.
[32] F.S. Lien, H. Liu, E. Chui, C.J. McCartney, Flow Turb. Combust. 83 (2009) 205–226.
[33] M. de Joannon, A. Cavaliere, T. Faravelli, E. Ranzi, P. Sabia, A. Tregrossi, Proc. Combust. Inst. 30 (2005) 2605–2612.
[34] M. de Joannon, A. Matarazzo, P. Sabia, A. Cavaliere, Proc. Combust. Inst. 31 (2007) 3409–3416.
[35] D.K. Lilly, Phys. Fluids 4 (1992) 633–635.
[36] M. Graça, A. Duarte, P. Coelho, M. Costa, Fuel Process. Technol. 107 (2012) 126–137.
[37] M.K. Bobba, P. Gopalakrishnan, K. Periagaram, J.M. Seitzman, AIAA Paper 2007-0173 (2007).
[38] V. Moureau, P. Domingo, L. Vervisch, Combust. Flame 158 (2011) 1340–1357.
[39] V. Moureau, P. Domingo, L. Vervisch, C. R. Mecanique 339 (2011) 141–148.
[40] A.J. Chorin, Math. Comput. 22 (1968) 745–762.
[41] H. Yamashita, M. Shimada, T. Takeno, Proc. Combust. Inst. 26 (1996) 27–34.
[42] P. Domingo, L. Vervisch, K. Bray, Combust. Theory Model. 6 (2002) 529–551.
[43] P. Domingo, L. Vervisch, J. Réveillon, Combust. Flame 140 (2005) 172–195.
[44] P. Nguyen, L. Vervisch, V. Subramanian, P. Domingo, Combust. Flame 157 (2010) 43–61.